Effects of Zeolite Structural Confinement on Adsorption Thermodynamics and Reaction Kinetics for Monomolecular Cracking and Dehydrogenation of *n*-Butane

Amber Janda,[†] Bess Vlaisavljevich,[†] Li-Chiang Lin,[‡,⊥] Berend Smit,[†,§] and Alexis T. Bell*[,†]

[†]Department of Chemical and Biomolecular Engineering, University of California—Berkeley, Berkeley, California 94720, United States

[‡]Department of Process and Energy, Delft University of Technology, Leeghwaterstraat 39, 2628CB Delft, The Netherlands

[§]Institute of Chemical Sciences and Engineering, École Polytechnique Fédérale de Lausanne, Rue de l'Industrie 17, CH-1951 Sion, Switzerland

S *Supporting Information*

ABSTRACT: The effects of zeolite structure on the kinetics of *n*-butane monomolecular cracking and dehydrogenation are investigated for eight zeolites differing in the topology of channels and cages. Monte Carlo simulations are used to calculate enthalpy and entropy changes for adsorption (ΔH_{ads-H^+} and ΔS_{ads-H^+}) of gas-phase alkanes onto Brønsted protons. These parameters are used to extract intrinsic activation enthalpies ($\Delta H_{int}^{\ddagger}$), entropies ($\Delta S_{int}^{\ddagger}$), and rate coefficients (k_{int}) from measured data. As ΔS_{ads-H^+} decreases (i.e., as confinement increases), $\Delta H_{int}^{\ddagger}$ and $\Delta S_{int}^{\ddagger}$ for terminal cracking and dehydrogenation decrease for a given channel topology. These results, together with positive values observed for $\Delta S_{int}^{\ddagger}$, indicate that the transition states for these reactions resemble products. For central cracking (an earlier transition state), $\Delta H_{int}^{\ddagger}$ is relatively constant, while $\Delta S_{int}^{\ddagger}$ increases as ΔS_{ads-H^+} decreases because less entropy is lost upon protonation of the alkane. Concurrently, selectivities to terminal cracking and dehydrogenation decrease relative to central cracking because $\Delta S_{int}^{\ddagger}$ decreases for the former reactions. Depending on channel topology, changes in the measured rate coefficients (k_{app}) with confinement are driven by changes in k_{int} or by changes in the adsorption equilibrium constant (K_{ads-H^+}). Values of $\Delta S_{int}^{\ddagger}$ and $\Delta H_{int}^{\ddagger}$ are positively correlated, consistent with weaker interactions between the zeolite and transition state and with the greater freedom of movement of product fragments within more spacious pores. These results differ from earlier reports that $\Delta H_{int}^{\ddagger}$ and $\Delta S_{int}^{\ddagger}$ are structure-insensitive and that k_{app} is dominated by K_{ads-H^+}. They also suggest that ΔS_{ads-H^+} is a meaningful descriptor of confinement for zeolites having similar channel topologies.
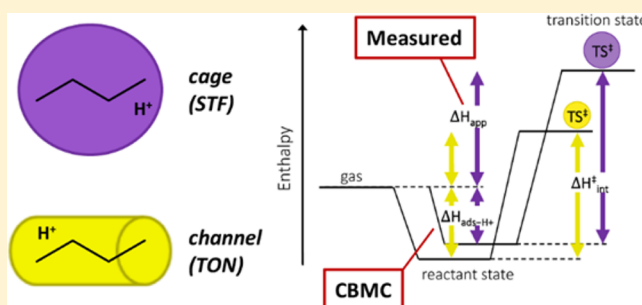
1. INTRODUCTION

Zeolites are microporous acid catalysts comprised of networks of AlO_4^- and SiO_4 tetrahedra that form pores of molecular size. The negative charge associated with each AlO_4^- unit is balanced by a catalytically active Brønsted proton, and the molecular dimensions of the pores impart zeolites with shape-selective properties that are exploited extensively in petroleum refining processes such as catalytic cracking.[1,2] Cracking occurs when an alkane (C_nH_{2n+2}) is converted into a smaller alkane and an alkene (C_mH_{2m+2} and $C_{n-m}H_{2(n-m)}$). Under industrial conditions, cracking occurs at high conversions and zeolitic Brønsted acid sites are mostly occupied by product alkenes. Under such conditions, cracking proceeds primarily via a complex bimolecular chain mechanism that includes transfer of hydride from alkanes to adsorbed alkenes, and oligomerization and β-scission of alkenes.[3,4]

At very low conversion, Brønsted acid sites are mostly unoccupied and cracking occurs by a monomolecular mechanism in which a C—C or C—H bond interacts with a proton to produce products of cracking (C_mH_{2m+2} and $C_{n-m}H_{2(n-m)}$) or dehydrogenation (H_2 and C_nH_{2n}), respectively.[5–10] By contrast to bimolecular cracking, monomolecular reaction kinetics are first-order overall and reaction rates are not typically limited by diffusion;[11–13] thus, apparent rate coefficients (k_{app}) can be readily obtained. In addition, because alkane molecules are activated directly by protons in the rate-determining step, kinetic parameters can be used to interpret the intrinsic effects of the active site environment on catalysis. As discussed below, the effects of active site environment on catalysis can be probed by varying the distribution of protons among different locations within a given zeolite, or by changing the zeolite framework itself.

Recent experimental work in our group has revealed that changes in the distribution of Al among channels and intersections of MFI that result from changes in the Si/Al

ratio are correlated with changes in the rates, selectivities, and activation parameters for n-butane cracking and dehydrogenation.[14] Variation in the intrinsic activation energies and entropies ($E_{int}^{\ddagger}$ and $\Delta S_{int}^{\ddagger}$) among these zeolites was concluded to contribute to differences in rates and selectivity and was attributed to differences in the confinement of transition states at channels versus intersections. Theoretical results reported by our group[15] support this interpretation and demonstrate that the intrinsic activation energy for a given reaction pathway of n-butane (e.g., central C−C cracking), as well as differences in $E_{int}^{\ddagger}$ between reaction pathways, depend on the location of Al in MFI.

By contrast, Gounder and Iglesia[16] have concluded that, for MOR, $E_{int}^{\ddagger}$ for monomolecular reactions of propane and butane is essentially insensitive to active site location and that k_{app} differs for 8-MR and 12-MR locations primarily because of differences in the entropy of adsorption. These authors attributed differences in selectivity to cracking vs dehydrogenation among 8- and 12-MR sites to "location-specific differences in entropy," which suggests that $\Delta S_{int}^{\ddagger}$ also depends on active site environment. Although this implication was not explicitly discussed by Gounder and Iglesia,[16] recent molecular dynamics simulations reported by Bučko and Hafner[17] indicate that $\Delta S_{int}^{\ddagger}$ for propane cracking is larger at 8-MR than at 12-MR sites in MOR. The above observations raise the question of whether the zeolite framework itself influences the intrinsic kinetics of monomolecular alkane reactions, since different framework types (e.g., MFI vs MWW) have different local environments for Brønsted acid sites. As discussed below, most previous studies have concluded that intrinsic kinetic parameters are insensitive to zeolite structure and, hence, that the effects of zeolite structure on k_{app} are due primarily to the effects of structure on the adsorption equilibrium.

Several authors have concluded that k_{app} for monomolecular conversion of n-hexane[18−20] and propane[21] increases with decreasing pore size for FAU, MOR, BEA, and MFI as a consequence of increases in the heat of adsorption. These authors have reported that $E_{int}^{\ddagger}$, calculated by subtracting the enthalpy of adsorption (ΔH_{ads}) from E_{app}, is nearly the same for the zeolites considered. While the value of $\Delta S_{int}^{\ddagger}$ was not addressed explicitly in these studies, van Bokhoven et al.[19] observed a linear correlation between the logarithm of the pre-exponential factor and E_{app} (a Constable plot) for monomolecular consumption of n-hexane. The authors suggested that the linearity of the Constable plot is caused by a linear correlation between the adsorption entropy (ΔS_{ads}) and ΔH_{ads}, while $E_{int}^{\ddagger}$ and the intrinsic pre-exponential factor are constant. Ramachandran et al.[22] later supported this proposal by observing that the slope of a plot of ΔS_{ads} vs ΔH_{ads}, measured experimentally for the zeolites investigated by van Bokhoven et al.,[19] was nearly equal to that of the Constable plot.

Gounder and Iglesia[16] have reported that values of $E_{int}^{\ddagger}$ for propane cracking and dehydrogenation are within experimental error for FER, MFI, and MOR. Differences in the values of $\Delta S_{int}^{\ddagger}$ among these zeolites can be seen in Table 3 of ref 16 (a result that is not discussed), although the authors suggested in later work[23] that the high density of charge on the transition state would preclude an influence of confinement on $\Delta S_{int}^{\ddagger}$. Gounder and Iglesia[23,24] have also concluded that differences in E_{app} and in the activation entropy (ΔS_{app}) between monomolecular reaction pathways are attributable to differences in the enthalpy or entropy of gas-phase reactant molecules protonated at different C−C or C−H bonds.

Based on this generalization, no influence of zeolite structure on selectivities would be expected. This conclusion, however, seems to contradict the authors' earlier report[16] that selectivity differences between 8-MR and 12-MR sites within MOR were caused by location-specific differences in transition-state entropy.

By contrast to the conclusions discussed above,[16,18−24] Kotrel et al.[25] have reported that $E_{int}^{\ddagger}$ for monomolecular cracking of n-hexane is somewhat larger for MFI than for BEA and FAU, although the difference was not attributed to zeolite structure. Instead, common to this and other studies mentioned above[16,18−25] is the assumption that differences in $E_{int}^{\ddagger}$ (if found) would reflect differences in acid strength, while the zeolite structure primarily influences the adsorption thermodynamics. The question then is whether zeolite structure has a significant effect on Brønsted acidity. If one uses the heat of protonation of NH_3 as a metric for acidity, then calculations of this quantity by Derouane and Chang[26] show that it differs by no more than 9 kJ mol^{-1} among highly siliceous zeolites having 8-, 10-, and 12-MR channels (FER, MFI, and MOR), suggesting that acidity is not a strong function of structural environment. However, similar acidity should not preclude an influence of confinement on intrinsic kinetics. Moreover, the earlier reports that $E_{int}^{\ddagger}$ is structure-independent[16,18−22] were based on calculations that used adsorption enthalpies measured well below the temperatures of reaction, and the adsorption was not always verified to take place exclusively at Brønsted sites. This practice compromises the accuracy of $E_{int}^{\ddagger}$ extracted from experimental data.[27] Thus, differences in $E_{int}^{\ddagger}$ among zeolites may have been missed in previous studies[16,18−22] in part because sufficiently accurate adsorption data were not available.

It can be seen from the above discussion that it is generally accepted that apparent kinetics vary among zeolite framework types because of changes in adsorption thermodynamic parameters, while $E_{int}^{\ddagger}$ depends on acid strength but not on the zeolite structure.[16,18−22] Some authors have also indicated that $\Delta S_{int}^{\ddagger}$ [19,22,23] and differences between $E_{int}^{\ddagger}$ or $\Delta S_{int}^{\ddagger}$ among reaction pathways[23,24] are also independent of zeolite structure. However, these conclusions contradict studies that suggest that $\Delta S_{int}^{\ddagger}$ [14,16,17] and $E_{int}^{\ddagger}$ [14,15] differ among locations within a given zeolite. It is the aim of this study to systematically investigate the effects of zeolite structure on monomolecular cracking and dehydrogenation kinetics for n-butane. Reaction kinetics are determined for eight zeolites having 10-MR channels and differing in channel topology and in the size and abundance of cavities. Monte Carlo simulations are used to determine the enthalpy and entropy changes for adsorption of gas-phase alkanes onto Brønsted protons (ΔH_{ads-H^+} and ΔS_{ads-H^+}) at reaction temperatures. These parameters are used to extract intrinsic activation enthalpies and entropies ($\Delta H_{int}^{\ddagger}$ and $\Delta S_{int}^{\ddagger}$) from measured activation parameters (ΔH_{app} and ΔS_{app}). The influence of zeolite structural confinement on each set of parameters is then examined, and the consequences of variations in activation parameters on the rates and selectivities for cracking and dehydrogenation are analyzed. Finally, the findings for n-butane are compared and contrasted with those obtained from an analysis of kinetic data for n-hexane monomolecular conversion reported by van Bokhoven et al.[19]

2. EXPERIMENTAL METHODS

2.1. Catalyst Preparation. MFI zeolites with nominal Si/Al ratios of 140, 40, 25, and 11.5 were obtained from Zeolyst International in the NH_4^+ form and were prepared as described in ref 14. To obtain the
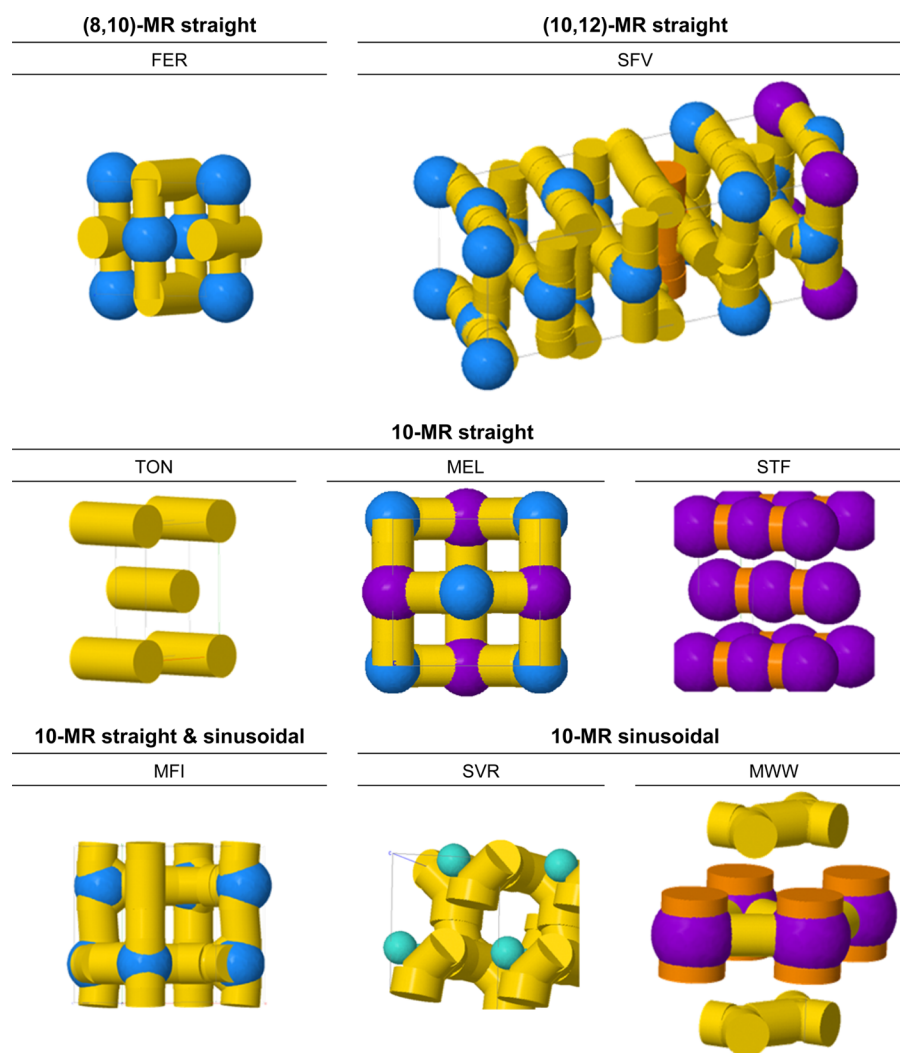
Figure 1. Representations of zeolite frameworks generated using the ZEOMICS web tool[33] for zeolites listed in Table 2. The channel topology (ring size and shape) is given in bold. Channels are shown in yellow (<6 Å diameter) and orange (>6 Å diameter). Cages are shown as green (<6 Å diameter), blue (6−8 Å diameter), and purple (>8 Å diameter) spheres.

H^+ forms of the zeolites, samples were heated to 773 K at a rate of 2 K min^{-1} in flowing air (100 cm^3 min^{-1}, zero grade, Praxair). Samples were held at 773 K for 4 h and then cooled (2 K min^{-1}) to room temperature.

FER with a nominal Si/Al ratio of 9 was obtained from Tosoh in the K$^+$ form (product HSZ-720 KOA). To convert to the NH$_4^+$ form, 3 g of the zeolite were stirred in 100 cm^3 of 1 M NH$_4$NO$_3$ aqueous solution for 6 h at 343 K, then filtered, dried, and rinsed with deionized water. This process was repeated twice for a total of three exchanges. The dried filtrate was then calcined in flowing synthetic air as described above for MFI to obtain the H$^+$ form.

Zeolites MEL, MFI, MWW, SFV, STF, SVR, and TON were synthesized by Chevron Energy Technology Co. (Richmond, CA) according to protocols described in the Supporting Information (section S.1). Because the distribution of Al atoms within the zeolite framework varies with the Si/Al ratio,[28] samples having different Si/Al ratios were synthesized (or obtained commercially) for zeolites having heterogeneous pore topologies consisting of multiple channel systems and cavities. (Measured kinetic parameters were appropriately averaged over the different samples for each framework type investigated.) After synthesis, in order to remove the organic structure-directing agents (SDAs), the zeolites were heated at 1 K min^{-1} in flowing synthetic air (100 cm^3 min^{-1}, zero grade, Praxair) to 393 K and held for 2 h. The temperature was then increased at 1 K min^{-1} to 873 K and held for 6 h before cooling to room temperature.

The samples were next exchanged twice using 1 M aqueous NH$_4$NO$_3$ (>60 cm^3 solution per g zeolite), dried, and calcined as described above for FER, to produce the H$^+$ forms.

2.2. Catalyst Structural and Textural Characterization. X-ray diffraction (XRD) patterns (included in the Supporting Information, section S.7) were collected using either a Bruker D8 Discover general area detector diffraction system (GADDS) or a Siemens D500 Powder XRD system, both of which are equipped with a Cu Kα X-ray source. Data were recorded digitally for 2θ values of 5° to 32°. Diffractograms were consistent with crystalline materials of the intended structure type. SEM images (not shown) were collected using a Hitachi S-5000 or a JEOL JSM 600F scanning electron microscope in order to determine characteristic particle sizes for use in the assessment of mass transfer limitations (see Supporting Information, section S.2). TEM images were also obtained (for TON only) using a FEI Tecnai 12 transmission electron microscope. The analysis presented in section S.2 demonstrates that, as for previous studies,[12−14,16,29] mass transfer does not limit the apparent rates of cracking and dehydrogenation (measured as described in section 2.4). Nitrogen adsorption isotherms were measured at 77 K using a Micromeritics Gemini VII apparatus, and micropore volumes were calculated using the t-plot method as described in ref 14.

2.3. Quantification of Al and Brønsted Proton Contents. Total Si and Al contents were determined by Galbraith Laboratories using inductively coupled plasma optical emission spectroscopy (ICP-

Table 1. Results of Characterization Experiments to Determine Al, Si, and H$^+$ (NH$_4^+$) Contents and N$_2$ Micropore Volumes (V_{micro})

sample[a]	source	Si/Al ratio	V_{micro} (cm^3 g^{-1})[b]		Al content (mmol g^{-1})	NH$_4^+$ content (mmol g^{-1})	NH$_4^+$/Al ratio
			meas.	literature			
FER-9	Tosoh	8.4	0.111	0.118–0.150[50–52]	1.71	1.92	1.12
MEL-22[c]	this work	22	0.146	0.110–0.150[50,52,53]	0.73	0.49	0.67
MEL-29	this work	29	0.142		0.54	0.51	0.94
MEL-35[c]	this work	35	0.141		0.46	0.30	0.65
MFI-24[c]	this work	24	0.131	0.120–0.147[32,54,55]	0.65	0.48	0.74
MFI-11.5	Zeolyst	12	0.138[14]		1.25	1.23	0.98
MFI-25	Zeolyst	29	0.132[14]		0.55	0.56	1.01
MFI-40	Zeolyst	44	0.130[14]		0.37	0.39	1.07
MFI-140	Zeolyst	142	0.131[14]		0.12	0.13	1.09
MWW-14	this work	14	0.144	0.130–0.180[29,55,56]	1.07	1.04	0.97
MWW-16	this work	16	0.169		0.99	0.96	0.97
MWW-18	this work	18	0.155		0.85	0.75	0.88
SFV-28	this work	28	0.128		0.57	0.51	0.89
SFV-51	this work	51	0.125		0.32	0.30	0.94
STF-18	this work	18	0.162	0.160[54]	0.85	0.78	0.92
SVR-71	this work	71	0.138	0.123[50]	0.23	0.24	1.06
SVR-84	this work	84	0.124		0.20	0.22	1.14
TON-49	this work	49	0.073	0.074,[57] 0.087[58]	0.33	0.28	0.84

[a]First three letters indicate IZA framework code, and number indicates nominal Si/Al ratio (for commercial samples) or measured Si/Al ratio (for experimental samples). [b]N$_2$ micropore volumes determined using the t-plot method. Representative literature values are listed once for each framework type. [c]Samples excluded from further analysis because of relatively low NH$_4^+$/Al ratio.

OES). To determine the concentration of Brønsted protons, the amount of NH$_3$ desorbed from NH$_4^+$-exchanged samples was quantified using online mass spectrometry. The zeolites used for this analysis were prepared by treating the corresponding H$^+$ forms with 1 M aqueous NH$_4$NO$_3$ as described in section 2.1 for FER. After drying in the open air, the NH$_4^+$ form zeolites (~50–170 mg) were then placed on a quartz wool bed within a cylindrical bubble (12.7 mm outer diameter) of a quartz reactor (6.5 mm outer diameter). The samples were heated in flowing He (20 cm^3 min^{-1}, 99.999%, Praxair) at 5 K min^{-1} and the effluent was monitored using a Varian 320-MS mass spectrometer. The amount of NH$_3$ desorbed was determined by integrating the signals for NH$_3$ (m/z 17) and water (m/z 18) and correcting the initial mass of catalyst for the amount of adsorbed water. The amount of H$^+$ was taken as equal to the moles of NH$_3$ desorbed because NH$_4^+$ ions exchange with Brønsted acid sites but not with Lewis acid sites.[19,30] The concentration of Lewis acid sites was not quantified because our previous work[14] and that of Gounder and Iglesia[16] have shown that the concentration of such sites, in zeolites prepared as described in section 2.1, does not correlate with monomolecular reaction rates.

2.4. Catalytic Rate Measurements. Rate data for monomolecular *n*-butane cracking and dehydrogenation over MFI were taken from ref 14. The procedures described therein were used to obtain rate data for all other zeolites used in the present work. Zeolite samples in the H$^+$ form (8 to 15 mg) were placed on a quartz wool bed within a tubular quartz reactor (6.5 mm outer diameter). The samples were heated at 5 K min^{-1} to 773 K in flowing 10% O$_2$ in He (50–100 cm^3 min^{-1}, 99.999%, Praxair) and held for 2 h prior to initiating reactions. The reaction rates were measured under differential conditions (<1.5% conversion), and the pressure drop across the reactor remained small (<10%) during rate measurements. The hydrocarbon content of feed and effluent streams was analyzed using a Varian CP-3800 gas chromatograph, and the amount of H$_2$ in the products was determined by performing an atom balance on C and H. Relative rates of *n*-butane diffusion and reaction were assessed as discussed in the Supporting Information (section S.2). The results of this analysis show that monomolecular reaction rates measured in this work were not limited by mass transport.

A transient period[14] was observed upon the initiation of reaction, during which rates and selectivities for cracking changed by less than

10%, with the exception of TON, for which the cracking rate decreased by 20%. For most samples, dehydrogenation rates decayed significantly with time on stream (TOS). For the reasons given in ref 14 and by other authors who have observed similar transient behavior for monomolecular dehydrogenation,[31,32] we suggest that a Lewis acid site is the cause of the initial dehydrogenation activity since cracking rates and selectivities do not change significantly with TOS. The somewhat greater loss of cracking activity for TON indicates that some of the one-dimensional pores (see Figure 1) become blocked by carbonaceous species on the crystal surface. Therefore, rate data were collected only after passage of this transient period.

Rate coefficients (normalized by the NH$_4^+$ concentration given in Table 1) and selectivities were obtained under steady-state conditions at 723–788 K for fixed space times (fixed total flow rates). Measured rate coefficients were extrapolated to zero space time in order to obtain values corresponding to conditions of zero conversion. This procedure is necessary because some active sites are inhibited by butene products even at very low conversion.[14] Ratios of product pairs (C$_2$H$_6$/C$_2$H$_4$, CH$_4$/C$_3$H$_6$, H$_2$/C$_4$H$_8$) and small but detectable rates of secondary processes (hydride transfer, oligomerization) tended to 1.0 and 0, respectively, in the limit of zero space time.

3. CONFIGURATIONAL-BIAS MONTE CARLO (CBMC) SIMULATIONS

3.1. Force Field Parameterization. The Lennard–Jones type potential developed by Dubbeldam et al.[34,35] was used to model the interaction between linear C3 to C6 alkanes and nonacidic O atoms of the zeolite framework. This potential was developed for all-silica zeolites and uses a united atom model to represent methyl (–CH$_3$) and methylene (–CH$_2$–) groups. The TraPPE model[36] was adopted for linear alkanes to describe nonbonded intermolecular interactions and intramolecular interactions including bond stretching, bending and torsion, and 1–4 van der Waals potentials. The Lennard–Jones parameters used to model the interactions of an alkane molecule with Brønsted acid sites were modified from those reported by Swisher et al.[37] (see Supporting Information, section S.3). In the present work, the force field was

parametrized using FAU, which has only one crystallographically distinct T-site; thus, the Al atoms occupied equivalent T-sites in the simulation and in the zeolite sample used by Eder et al.[38] to measure the enthalpy of adsorption (ΔH_{ads}) calorimetrically. A single "effective" potential was used for the four O atoms attached to an Al atom because protons move rapidly among the O atoms at temperatures of cracking catalysis.[39,40]

To perform the simulations, Zeo++[41] was used to distribute Al atoms randomly in a unit cell of FAU, such that the Si/Al of the unit cell was 2.7 (the same Si/Al ratio as that of the sample used to measure[38] ΔH_{ads}). The coordinates of the zeolite framework atoms were taken from the database of the International Zeolite Association (IZA) and the values used in each simulation are included with the Supporting Information in a compressed file folder. Values of ΔH_{ads} were then calculated for linear C3 to C6 alkanes at 323 K using, as a starting point, the parameters reported by Dubbeldam et al.[34] for the interaction of alkane united atoms with nonacidic O atoms. The value of epsilon was multiplied by a scaling factor which was varied until ΔH_{ads} was, on average, within 0.1 kJ mol^{-1} of the measured enthalpy of adsorption. To validate the transferability of the force field parameters, ΔH_{ads} was also calculated for propane and *n*-butane in CHA (see Supporting Information, section S.3). Simulated values were in excellent agreement with measured values reported by Barrer and Davies.[42] The parametrization described above differs from that described by Swisher et al.[37] for MFI. In the latter work, the unit cell contained one Al atom (corresponding to a Si/Al ratio of 95), while the Si/Al ratio of the sample used to measure ΔH_{ads} was 35.[38] In addition, only one of the four associated O atoms was treated as acidic.

It is noted that the value of ΔH_{ads} corresponds to an ensemble average for adsorption at Brønsted protons and at nonacidic parts of the zeolite. For the extraction of intrinsic activation barriers from apparent values using eqs 6 and 7, the adsorption enthalpy and entropy for the subset of molecules located at Brønsted protons must be evaluated. The procedure for determining these quantities using the above force field parameters is described in section 3.2.

3.2. Calculation of $\Delta H_{ads\text{-}H+}$ and $\Delta S_{ads\text{-}H+}$ for Alkanes in a Reactant State. A one-step approach using the Widom particle insertion method[43] with domain decomposition was used to efficiently compute the enthalpy and entropy changes for adsorption of alkane molecules from the gas phase onto Brønsted protons ($\Delta H_{ads\text{-}H+}$, $\Delta S_{ads\text{-}H+}$). CBMC simulations were performed as described in previous studies to calculate values of the Henry coefficient (K_H) and ΔH_{ads}.[27,37,44] As noted in section 3.1, these quantities correspond to adsorption anywhere within the zeolite pores. A subset of the adsorbed molecules are in a reactant state at Brønsted protons, defined as a configuration in which a C−C bond j is located within 5 Å of an Al atom located at T-site i.[37] To determine adsorption enthalpies and Henry coefficients ($\Delta H_{ads\text{-}H+}(i,j)$ and $K_{H-H+}(i,j)$) for this subset of molecules, a domain decomposition was performed by assigning each insertion to the reactant or nonreactant state. The internal energy change of adsorption ($\Delta U_{ads\text{-}H+}(i,j)$) was computed directly from the ensemble-averaged energies of molecules in the reactant state, and $\Delta H_{ads\text{-}H+}(i,j)$ was then calculated from the equation $\Delta H_{ads\text{-}H+}(i,j) = \Delta U_{ads\text{-}H+}(i,j) - RT$. The entropy of adsorption was obtained from the equation,[27]

$$\Delta S_{ads-H+}(i, j) = R \ln\left[\frac{RT}{V_{H+}n_{H+}}K_{H-H+}(i, j)\right] + \frac{\Delta U_{ads-H+}(i, j)}{T} \tag{1}$$

where n_{H+} is the moles of protons per kg of zeolite and V_{H+} is the total volume contained in 1 mol of reactant state spheres of radius 5 Å. The Henry coefficient for the reactant state, $K_{H-H+}(i,j)$, is related to the dimensionless equilibrium constant, $K_{ads\text{-}H+}(i,j)$, according to

$$\frac{RT}{V_{H+}n_{H+}}K_{H-H+}(i, j) \equiv K_{ads-H+}(i, j) = \exp\left(-\frac{\Delta A_{ads-H+}(i, j)}{RT}\right) \tag{2}$$

where $\Delta A_{ads\text{-}H+}$ is the Helmholtz free energy of adsorption (see ref 27, Supporting Information sections S.1−S.2).

The values of $\Delta H_{ads\text{-}H+}$ and $\Delta S_{ads\text{-}H+}$ were computed at 773 K as described above for zeolites MFI, MWW, TON, SFV, FER, SVR, STF, and MEL with one Al atom (one Brønsted proton) per unit cell. Several million insertions were carried out to ensure statistically accurate ensemble averages. Analogous simulations were performed for each T-site symmetry i, and expected values of $\Delta H_{ads\text{-}H+}(j)$ and $\Delta S_{ads\text{-}H+}(j)$ for zeolites having a random distribution of Al were calculated as the Boltzmann averages over all T-sites i (see ref 27, section S.3), taking into account the multiplicity of each T-site symmetry i within the unit cell. Values of $\Delta H_{ads\text{-}H+}$ and $\Delta S_{ads\text{-}H+}$, averaged over all bonds j, were taken as the Boltzmann averages of $\Delta H_{ads\text{-}H+}(j)$ and $\Delta S_{ads\text{-}H+}(j)$. To independently verify that $\Delta S_{ads\text{-}H+}$ obtained from simulations is in agreement with experiments, simulated values must be compared to adsorption entropies determined from experimental data for which adsorption is verified to take place exclusively at Brønsted protons. In our previous work,[27] good agreement was found between values of $\Delta S_{ads\text{-}H+}$ determined from simulations and from experiments for the adsorption of linear alkanes in MFI at ∼300−400 K. The main source of uncertainty in simulated values of $\Delta S_{ads\text{-}H+}$ is the choice of the cutoff radius for the reactant state. Because the distance between alkanes and Brønsted protons involved in a specific interaction is likely to be similar for different zeolites, differences in $\Delta S_{ads\text{-}H+}$ between different zeolites are not expected to be significantly influenced by uncertainty in the cutoff radius.

It is noted that, previously,[27] $\Delta H_{ads\text{-}H+}(i,j)$ and $\Delta S_{ads\text{-}H+}(i,j)$ were obtained from two sets of simulations. First, the Widom particle insertion method was used to determine K_H. Next, simulations were performed in the canonical (NVT) ensemble to calculate the probability of finding the alkane in a reactant state ($P_{react}(i,j)$) and the value of $\Delta U_{ads\text{-}H+}(i,j)$ for molecules in the reactant state by storing the data every 100 MC steps and then postprocessing the data. The value of $\Delta S_{ads\text{-}H+}$ was determined from eq 1, where $K_{H-H+}(i,j) = P_{react}K_H$ (see ref 27, eq 9); P_{react} represents the probability that an adsorbed molecule is in a reactant state. The computational cost associated with implementing the newer methodology is significantly lower than that for the two-step approach. Values of $\Delta H_{ads\text{-}H+}(i,j)$ and $\Delta S_{ads\text{-}H+}(i,j)$ obtained using each method were compared and were found to be identical.

4. RESULTS AND DISCUSSION

4.1. Elementary Steps of Monomolecular Cracking and Dehydrogenation. Before presenting an analysis of the

effects of zeolite structure and confinement on monomolecular cracking and dehydrogenation, it is useful to briefly outline the elementary steps involved in these processes. A detailed derivation of the equations presented below can be found in ref 27. First, alkane molecules are adsorbed from the gas phase into the zeolite pores at quasi-equilibrium. A fraction of the adsorbed molecules are located near Brønsted protons and are in a "reactant state," defined as any configuration in which a C−C bond is located within 5 Å of an Al atom.[37] The dimensionless thermodynamic equilibrium constant for this subset of molecules is defined as[27]

$$K_{ads-H+} = \exp\left(-\frac{\Delta A_{ads-H+}}{RT}\right)$$

(3)

where $\Delta A_{ads\text{-}H+}$ is the Helmholtz free energy change for adsorption from the gas phase to the reactant state. The value of $\Delta A_{ads\text{-}H+}$ is equal to $\Delta U_{ads\text{-}H+} - T\Delta S_{ads\text{-}H+}$, where $\Delta U_{ads\text{-}H+}$ and $\Delta S_{ads\text{-}H+}$ are the energy and entropy of adsorption. The enthalpy of adsorption, $\Delta H_{ads\text{-}H+}$, is equal to $\Delta U_{ads\text{-}H+} - RT$.[27]

Once in a reactant state, alkane molecules undergo cracking or dehydrogenation in the rate-determining step. The intrinsic rate coefficient for the reaction is given by absolute rate theory as

$$k_{int} = \frac{k_B T}{h} \exp\left(-\frac{\Delta G_{int}^{\ddagger}}{RT}\right)$$

(4)

where $\Delta G_{int}^{\ddagger}$ (the intrinsic Gibbs free energy of activation) is equal to $\Delta H_{int}^{\ddagger} - T\Delta S_{int}^{\ddagger}$, and $\Delta H_{int}^{\ddagger}$ and $\Delta S_{int}^{\ddagger}$ are the intrinsic enthalpy and entropy of activation. The apparent first-order rate coefficient, k_{app}, is related to k_{int} and $K_{ads\text{-}H+}$ according to

$$k_{app} = \frac{V_{H^+}}{RT} k_{int} K_{ads-H+} = \frac{v_{H^+}}{h} \exp\left(-\frac{\Delta A_{ads-H+} + \Delta G_{int}^{\ddagger}}{RT}\right)$$

(5)

where v_{H^+} is the volume of a single reactant state sphere and V_{H^+} (upper case) is the volume of 1 mol of such spheres. The term inside the exponential of eq 5 can be expanded into the apparent enthalpy and entropy of activation (ΔH_{app} and ΔS_{app}) as follows:

$$\Delta H_{app} = \Delta H_{ads-H+} + \Delta H_{int}^{\ddagger} = -R\left[\frac{\partial \ln k_{app}}{\partial(1/T)}\right] - RT$$

(6)

$$\Delta S_{app} = \Delta S_{ads-H+} + \Delta S_{int}^{\ddagger} = R\left[\ln k_{app,T\rightarrow\infty} - \ln\frac{v_{H^+}}{h}\right]$$

(7)

where $\partial \ln k_{app}/\partial(1/T)$ and $\ln k_{app,T\rightarrow\infty}$ are the slope and intercept of an Arrhenius plot, respectively. Values of ΔH_{app} and ΔS_{app} can be determined from an Arrhenius plot or, as has been done in this work, by weighted nonlinear regression of rate data using eq 5 (see Supporting Information, section S.5). It can be seen from eqs 6 and 7 that ΔH_{app} and ΔS_{app} represent sums of adsorption thermodynamic parameters and intrinsic activation parameters.

Equations 6 and 7 show that intrinsic activation parameters ($\Delta H_{int}^{\ddagger}$ and $\Delta S_{int}^{\ddagger}$) can be obtained by subtracting values of $\Delta H_{ads\text{-}H+}$ and $\Delta S_{ads\text{-}H+}$ from experimentally measured values of ΔH_{app} and ΔS_{app}. In doing so, it is important that $\Delta H_{ads\text{-}H+}$ and $\Delta S_{ads\text{-}H+}$ correspond to the temperatures at which ΔH_{app} and ΔS_{app} are measured (>723 K). A few authors have reported

values of $\Delta H_{ads\text{-}H+}$ and $\Delta S_{ads\text{-}H+}$ determined experimentally for the adsorption of alkanes at Brønsted protons in some zeolites.[38,45,46] Using these values of $\Delta H_{ads\text{-}H+}$ and $\Delta S_{ads\text{-}H+}$ (measured at 300−400 K) to extract $\Delta H_{int}^{\ddagger}$ and $\Delta S_{int}^{\ddagger}$ from rate data measured above 700 K does not properly account for the redistribution of alkane to active sites located in different parts of the zeolite, or the different ensemble of reactant-state configurations for a given active site, at higher temperatures.[9,27,47−49] Since experimental adsorption measurements are not possible at reaction temperatures, the values of $\Delta H_{ads\text{-}H+}$ and $\Delta S_{ads\text{-}H+}$ in this work are calculated using CBMC simulations (see section 3) and used to obtain $\Delta H_{int}^{\ddagger}$ and $\Delta S_{int}^{\ddagger}$ from eqs 6 and 7.

4.2. Catalyst Characterization. The results of catalyst characterization experiments are summarized in Table 1. Representative values for the N_2 micropore volumes (V_{micro}) taken from the literature are included for comparison and are similar to measured micropore volumes, suggesting that zeolite pores that are not occluded by extraframework debris. The ratio of NH_4^+ to Al is within ~15% of 1.0 with the exception of MEL-22, MEL-35, and MFI-24, for which the ratio is 0.65−0.74. This finding indicates that, with the exception of the latter three samples, at least ~85% of the Al atoms reside in framework positions and are associated with Brønsted protons for zeolites in the H+ form. Sites that do not exchange NH_4^+ are likely associated with extraframework Al (EFAl). Because EFAl can potentially influence reaction rates,[19] MEL-22, MEL-35, and MFI-24 were excluded from the analysis of kinetic data presented in section 4.4. Although EFAl is not believed to be absent from the remaining samples, its content is expected to be low, as noted above. More importantly, there is no apparent correlation between the NH_4^+/Al ratio (and, by inference, EFAl content) in Table 1 and various descriptors of structural confinement included in Table 2. Thus, any influence of EFAl on reaction kinetics should not confound interpretations of the influence of confinement on kinetics.

4.3. Adsorption Thermodynamics. We next discuss the influence of zeolite structure and confinement on the enthalpy and entropy of adsorption for *n*-butane in a reactant state

Table 2. Topological Characteristics of Zeolite Frameworks Including Number of T-Atoms Circumscribing the Channels, Pathways Traced by Channels, Diameter of Largest Cavity, and Percentage of Pore Volume Present in Cages

framework type	channels		cavities	
	ring size (T atoms)	channel pathway	largest cavity diameter[a] (Å)	percentage of pore volume in cages[b]
FER	8	straight	7.0	47
	10	straight		
MEL	10	straight	8.4	40
MFI	10	sinusoidal	7.0	26
	10	straight		
MWW	10	sinusoidal	10.3	27
SFV	10	straight	8.3	19
	12	straight		
STF	10	straight	8.3	85
SVR	10	sinusoidal	5.7	21
TON	10	straight	−	0

[a]Size of largest included sphere calculated by First et al.[33] [b]Fraction of pore volume present in accessible cavities or cages.[33]
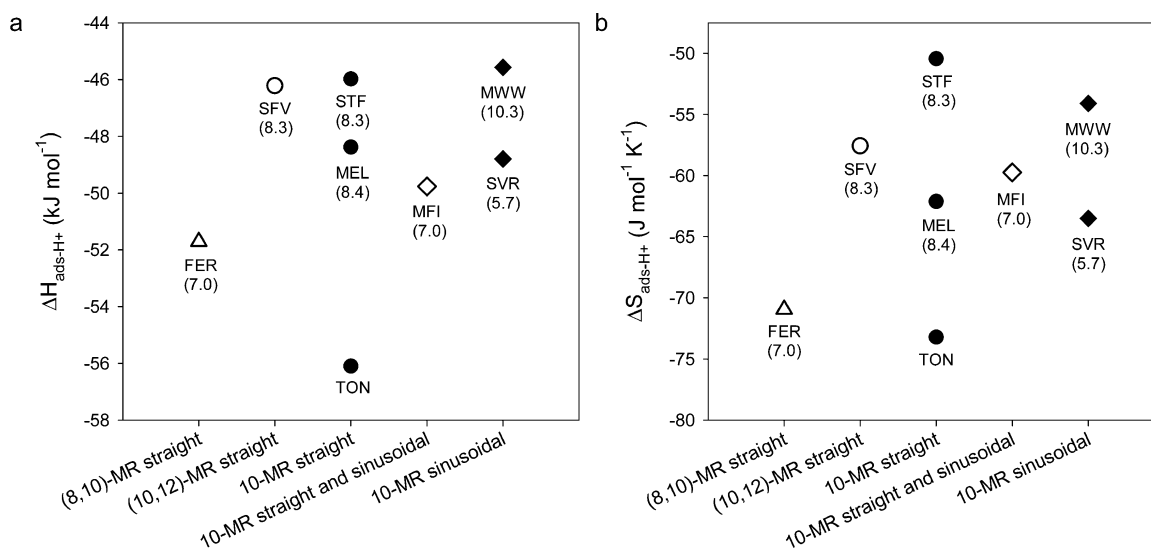
Figure 2. (a) Enthalpy and (b) entropy of adsorption at 773 K, determined using CBMC simulations, for *n*-butane in a reactant state within zeolites listed in Table 2. The largest cavity diameter (Å) is indicated below each data point except for TON, which does not contain cages.

Table 3. Adsorption Equilibrium Constant (K_{ads-H+}) and Enthalpies and Entropies of Adsorption for *n*-Butane Adsorbed in a Reactant State via Terminal ($j = 1$) and Central ($j = 2$) C−C Bonds, and Boltzmann Averages over All C−C Bonds, Determined Using CBMC Simulations at 773 K[a]

| framework type	$\langle K_{ads-H+} \rangle$			$\langle \Delta H_{ads-H+} \rangle$ (kJ mol^{-1})			$\langle \Delta S_{ads-H+} \rangle$ (J mol^{-1} K^{-1})		
	$j = 1$	$j = 2$	ave.	$j = 1$	$j = 2$	ave.	$j = 1$	$j = 2$	ave.
FER	0.23	0.22	0.23	−51.7	−51.7	−51.7	−70.8	−71.2	−70.0
TON	0.33	0.35	0.34	−56.1	−56.1	−56.1	−73.3	−73.0	−73.2
SVR	0.36	0.33	0.35	−48.8	−48.7	−48.8	−63.3	−63.9	−63.5
MEL	0.40	0.35	0.39	−48.4	−48.4	−48.4	−61.8	−62.9	−62.1
SFV	0.50	0.43	0.48	−46.2	−46.2	−46.2	−57.2	−58.4	−57.6
MFI	0.67	0.59	0.64	−49.7	−49.8	−49.8	−59.4	−60.5	−59.7
MWW	0.70	0.57	0.66	−45.5	−45.7	−45.6	−53.5	−55.6	−54.1
STF	1.22	0.83	1.09	−46.1	−45.7	−46.0	−49.6	−52.4	−50.5

[a]Each quantity corresponds to a random distribution of Al and accounts for the multiplicity of each T-site symmetry within the unit cell.

(ΔH_{ads-H+} and ΔS_{ads-H+}), determined using CBMC simulations as described in section 3. Visual representations of the eight zeolite frameworks are presented in Figure 1. Descriptors that affect confinement of *n*-butane are given in Table 2. These descriptors include the number of T atoms comprising the channel openings, the paths traced by the channels (e.g., straight, sinusoidal), the largest cavity diameter (LCD),[33] and the percentage of pore volume present in cages (defined as voids for which the included sphere diameter exceeds the diameter of connected channels). It can be seen that the zeolites comprise 10-MR channels and differ primarily in the size and prevalence of cages and in the paths traced by the channels. In addition, the LCD for all zeolites that possess cages is nearly as large as, or exceeds, the diameter of gyration of *n*-butane perpendicular to its long axis (7.67 Å), which indicates that there is sufficient space for relatively free rotation within the cages.[59] Therefore, *n*-butane and transition states that originate from reactant-state *n*-butane are expected to experience greater freedom of movement in the cages than in the channels of these zeolites.

In addition to the presence of cages, the channel topology is also expected to affect the confinement of adsorbates. For example, Monte Carlo simulations show that the adsorption of gas-phase alkanes into zeolite channels imposes significant conformational changes on alkane molecules and that these changes can differ considerably among channel topologies (e.g., straight vs sinusoidal; 8-MR vs 10-MR).[60−63] Adsorption into cages results in far less conformational change, especially when the cages are larger in diameter than the length of the molecules.[61−63] Therefore, details of the cage geometry other than a characteristic size (LCD) are expected to be less consequential to confinement, and the specific modes of motion that are accessible to the adsorbate, than is channel topology. Thus, the effects of descriptors given in Table 2 on confinement and adsorption thermodynamics are presented below for sets of zeolites that share the same channel topology given in Table 2, but that differ in the size or prevalence of cages. A detailed investigation of the effects of channel geometry on adsorption thermodynamics is the subject of a future publication.

The values of ΔH_{ads-H+} and ΔS_{ads-H+} are plotted in Figure 2 in groups corresponding to different channel systems. The LCD values listed in Table 2 are shown below the data points. Examination of the data corresponding to 10-MR straight channels in Figure 2 reveals that increasing the percentage of pore volume in cages of similar LCD (8.3−8.4 Å) from 0% to 40% to 85% (e.g., going from TON to MEL to STF) decreases the magnitudes of ΔH_{ads-H+} and ΔS_{ads-H+}. This trend is consistent with the greater freedom of movement and the weaker van der Waals interactions of *n*-butane with the zeolite
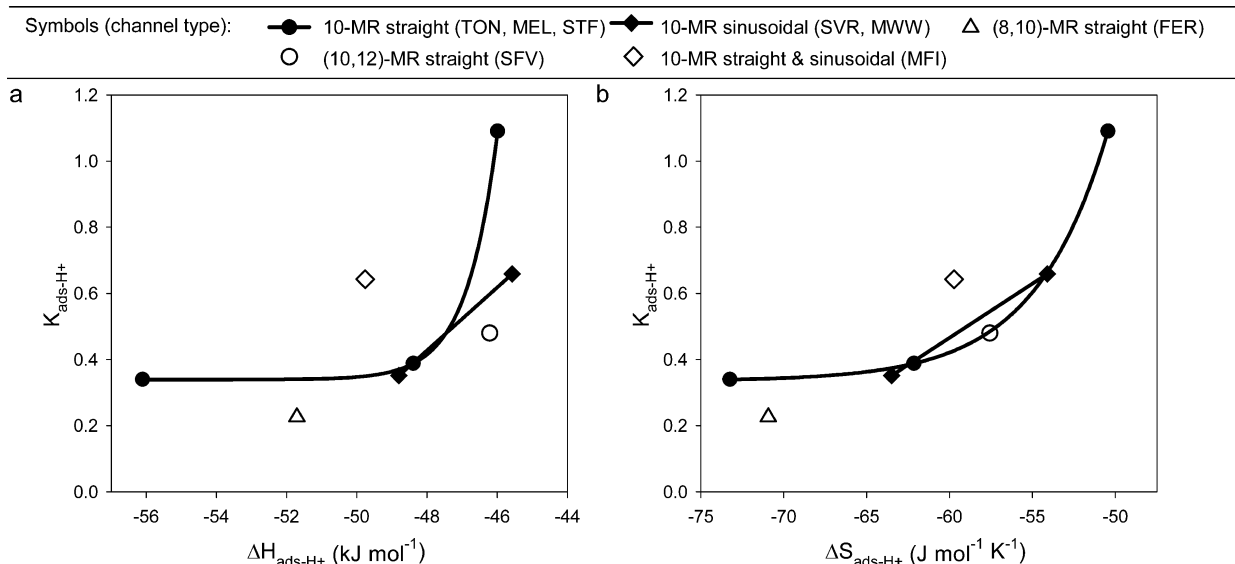
Figure 3. Equilibrium constant for adsorption of *n*-butane in a reactant state vs (a) enthalpy of adsorption and (b) entropy of adsorption. All quantities were determined using CBMC simulations at 773 K.

in the cages (∼8.4 Å diameter) versus in the channels (∼5.5 Å diameter)[64,65] and, therefore, with a decrease in confinement. Comparison of the point for SFV, which has both 10- and 12-MR straight channels, with that for MEL, which has a similar topology to SFV[66] but only 10-MR straight channels, shows that introducing 12-MR channels decreases confinement because ΔH_{ads-H+} and ΔS_{ads-H+} are somewhat less negative for SFV than for MEL. The effect of increasing the LCD at similar percent pore volume in cages and similar channel shape can be seen by comparing the data points for SVR (LCD = 5.7 Å) and MWW (LCD = 10.3 Å), which have 10-MR sinusoidal channel systems; ΔH_{ads-H+} and ΔS_{ads-H+} are less negative for MWW than for SVR. The above results demonstrate the importance of the size and prevalence of cages to confinement and that these structural features correlate with ΔH_{ads-H+} and ΔS_{ads-H+}.

It is also interesting to examine the dependence of the equilibrium constant for adsorption (K_{ads-H+}) on ΔS_{ads-H+} and ΔH_{ads-H+} as well as the correlation between ΔS_{ads-H+} and ΔH_{ads-H+}, since the slope of this correlation and that of a plot of ΔS_{app} vs ΔH_{app} will be equal if $\Delta H_{int}^{\ddagger}$ and $\Delta S_{int}^{\ddagger}$ are constant, and since previous reports indicate that the adsorption equilibrium is controlled by enthalpy. The values of ΔH_{ads-H+}, ΔS_{ads-H+}, and K_{ads-H+} for *n*-butane adsorption via a terminal or central bond ($j = 1$ or $j = 2$, respectively), and the Boltzmann average over all three C−C bonds, are given in Table 3. Values of K_{ads-H+} shown in Table 3 are plotted vs ΔH_{ads-H+} and vs ΔS_{ads-H+} in Figure 3a and 3b, respectively. It can be seen that K_{ads-H+} generally increases as both ΔH_{ads-H+} and ΔS_{ads-H+} become less negative (i.e., as confinement decreases). These findings differ from the report that the concentration of alkane within the zeolite increases with the heat of adsorption (for MFI, MOR, BEA, and FAU), leading to a greater rate of cracking.[18−21] We will show in section 4.5, however, that the dependence of K_{ads-H+} on ΔH_{ads-H+} and ΔS_{ads-H+} depends on the set of zeolites chosen for comparison and is not, in general, dominated by either parameter.

Figure 4 shows a plot of ΔS_{ads-H+} vs ΔH_{ads-H+}, with an arrow showing the direction of increasing confinement. It can be seen that ΔS_{ads-H+} generally decreases as ΔH_{ads-H+} decreases, consistent with the observations of Ramachandran et al. for
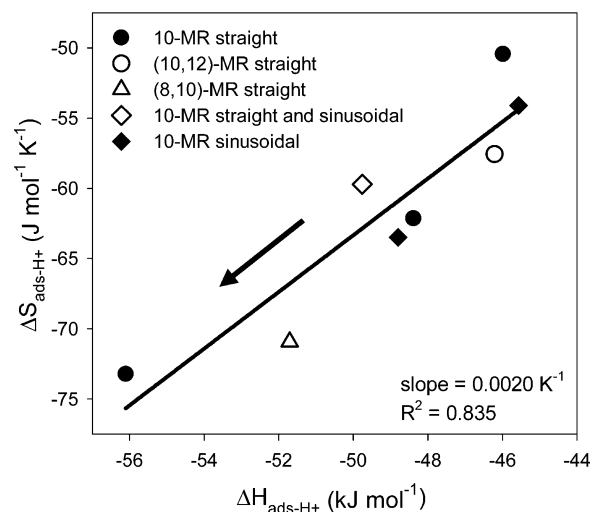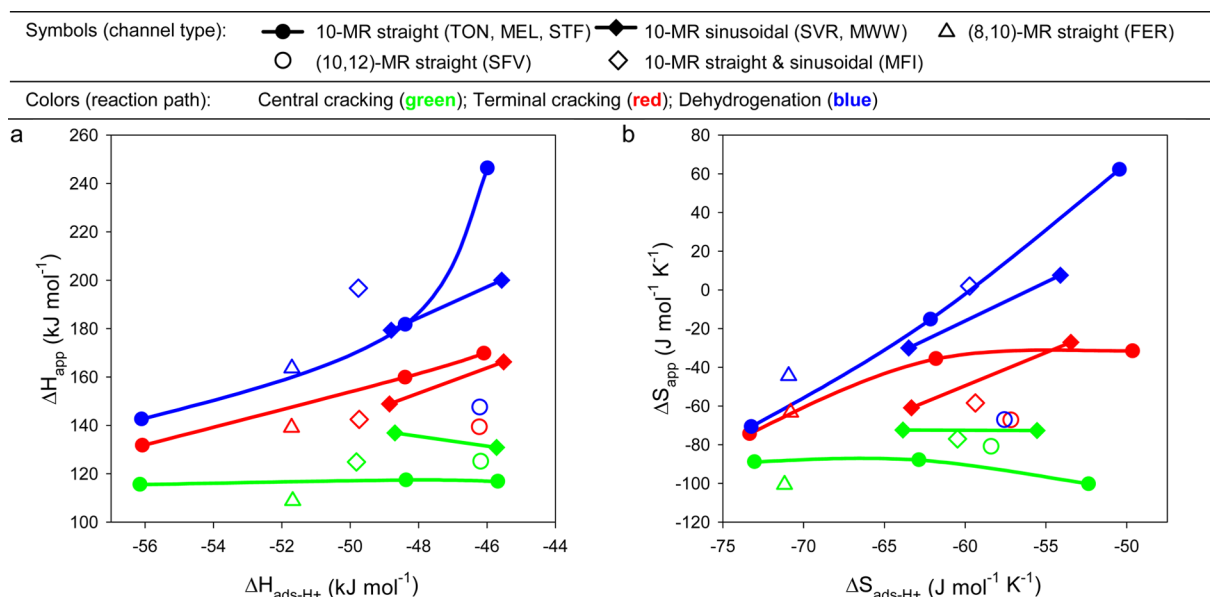

Figure 4. Entropy of adsorption vs enthalpy of adsorption for *n*-butane in a reactant state at 773 K, determined using CBMC simulations, for zeolites listed in Table 2. The slope and R^2 values of a linear fit of the data are included on the plot. The arrow indicates the general direction of increasing confinement.

n-hexane adsorption in MFI, MOR, and FAU.[22] The slope of a linear fit of the data included in Figure 4 is ∼0.0020 K^{-1}, which is larger than the slope reported in ref 22 (∼0.0013 K^{-1}). This finding is consistent with the larger channels and cavities of the zeolites investigated for *n*-hexane; FAU and MOR possess 12-MR channels, and FAU comprises cages 12 Å in diameter. By contrast, the pore dimensions of the zeolites in Table 2 are smaller and would more strongly restrict local motion of the adsorbate. The loss of such motion would affect entropy more strongly than enthalpy, leading to a larger slope for a plot of ΔS_{ads-H+} vs ΔH_{ads-H+}. This interpretation is consistent with the observation of Eder and Lercher[67] that the slope of ΔS_{ads-H+} vs ΔH_{ads-H+} for linear alkanes adsorbed within a given zeolite increased with decreasing pore size.

4.4. Influence of Zeolite Structure on Kinetics of *n*-Butane Cracking and Dehydrogenation. *4.4.1. Effects of*

Figure 5. Plots of (a) apparent activation enthalpy vs enthalpy of adsorption and (b) apparent activation entropy vs entropy of adsorption for *n*-butane monomolecular reactions at 773 K. Values of $\Delta H_{ads\text{-}H+}$ and $\Delta S_{ads\text{-}H+}$ were determined from CBMC simulations, and ΔH_{app} and ΔS_{app} from measured rate data. Representative 95% confidence intervals for ΔH_{app} and ΔS_{app} are ± 7 kJ mol^{-1} and ± 9 J mol^{-1} K^{-1} for cracking, and ± 8 kJ mol^{-1} and ± 11 J mol^{-1} K^{-1} for dehydrogenation.
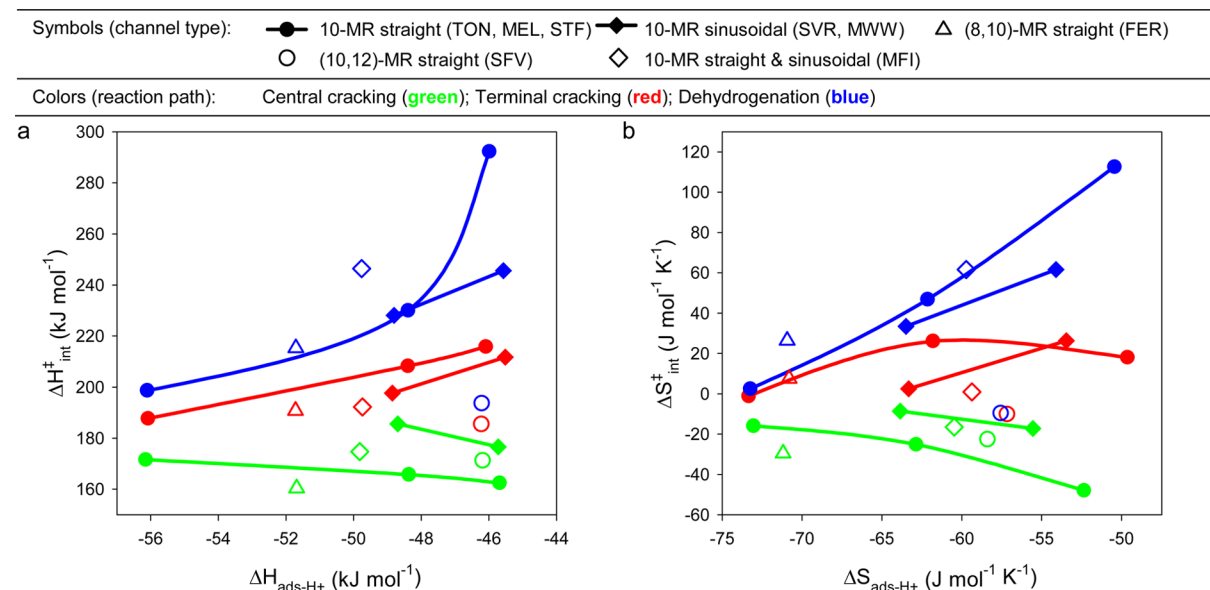
Figure 6. Plots of (a) intrinsic activation enthalpy vs enthalpy of adsorption and (b) intrinsic activation entropy vs entropy of adsorption for *n*-butane monomolecular reactions at 773 K. Values of $\Delta H_{ads\text{-}H+}$ and $\Delta S_{ads\text{-}H+}$ were determined from CBMC simulations and used to extract $\Delta H_{int}^{\ddagger}$ and $\Delta S_{int}^{\ddagger}$ from experimental data using eqs 6 and 7. Representative 95% confidence intervals for $\Delta H_{int}^{\ddagger}$ and $\Delta S_{int}^{\ddagger}$ are ± 7 kJ mol^{-1} and ± 9 J mol^{-1} K^{-1} for cracking, and ± 8 kJ mol^{-1} and ± 11 J mol^{-1} K^{-1} for dehydrogenation.

Zeolite Structure on Apparent and Intrinsic Activation Parameters. We begin our discussion of the effects of zeolite structure on the kinetics of cracking and dehydrogenation by examining the apparent and intrinsic activation parameters. The effects of confinement on these parameters can be interpreted more directly than can the effects of confinement on rate coefficients and selectivities (discussed in sections 4.4.2 and 4.4.3), which depend on the free energy of activation. We first recall that measured activation parameters (ΔH_{app} and ΔS_{app}) are equal to sums of thermodynamic adsorption parameters ($\Delta H_{ads\text{-}H+}$ and $\Delta S_{ads\text{-}H+}$) and intrinsic activation barriers ($\Delta H_{int}^{\ddagger}$ and $\Delta S_{int}^{\ddagger}$; see section 4.1 and eqs 6 and 7). As noted in section

4.3, the values of $\Delta H_{ads\text{-}H+}$ and $\Delta S_{ads\text{-}H+}$ reflect the size and abundance of cages for a given channel topology (e.g., 10-MR straight, 10-MR sinusoidal) and, therefore, the level of confinement of adsorbates. We will use these parameters to represent changes in confinement for the different channel systems given in Table 2. As noted in the Introduction, previous studies have concluded that variation in ΔH_{app}[16,18−22] and ΔS_{app}[19,22,23] among zeolites is due to variation in the adsorption enthalpy and entropy, while intrinsic activation parameters are nearly constant. If this proposal were true in general, then eqs 6 and 7 predict that plots of ΔH_{app} vs
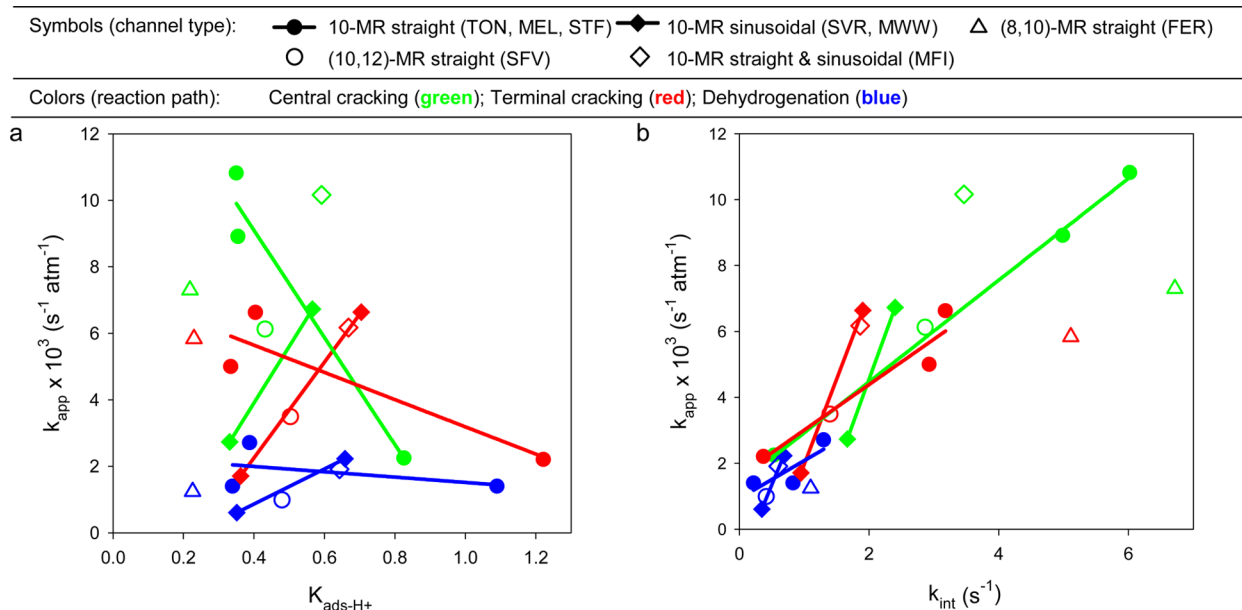
Figure 7. Plot of apparent (measured) first-order rate coefficients for *n*-butane monomolecular reactions at 773 K vs (a) equilibrium constant for adsorption to a reactant state (determined using CBMC simulations), and (b) intrinsic rate coefficient calculated using eq 4 and values of $\Delta H_{int}^{\ddagger}$ and $\Delta S_{int}^{\ddagger}$ shown in Figure 6. Values of k_{app} correspond to the arithmetic average for different Si/Al ratios listed in Table 1. Representative 95% confidence intervals for rate coefficients are ±8% for cracking and ±9% for dehydrogenation.

ΔH_{ads-H+} and ΔS_{app} vs ΔS_{ads-H+} for each reaction pathway should be linear and have slopes equal to 1.

Plots of ΔH_{app} vs ΔH_{ads-H+} and ΔS_{app} vs ΔS_{ads-H+} are presented in Figure 5a and 5b, respectively. (The values of ΔH_{app} and ΔS_{app} for MWW, MFI, and SVR correspond to Boltzmann averages over all Si/Al ratios in Table 1. Values for individual samples are included in the Supporting Information, section S.4.) It can be seen that, within a given channel topology, ΔH_{app} and ΔS_{app} for central cracking exhibit no discernible dependence on confinement, whereas the activation barriers for terminal cracking and for dehydrogenation generally decrease as confinement increases and ΔH_{ads-H+} and ΔS_{ads-H+} become more negative. In addition, the ranges observed for ΔH_{app} and ΔS_{app} differ from those observed for ΔH_{ads-H+} and ΔS_{ads-H+}, and therefore, the slopes of the plots in Figure 5 are not all equal to 1. It can thus be inferred that $\Delta H_{int}^{\ddagger}$ and $\Delta S_{int}^{\ddagger}$ vary significantly with changes in confinement.

To test this hypothesis, values of $\Delta H_{int}^{\ddagger}$ and $\Delta S_{int}^{\ddagger}$ for each reaction pathway were calculated, using eqs 6 and 7, by subtracting $\Delta H_{ads-H+}(j)$ or $\Delta S_{ads-H+}(j)$ determined from CBMC simulations (Table 3) from ΔH_{app} and ΔS_{app}. (The Boltzmann averages of $\Delta H_{ads-H+}(j)$ and $\Delta S_{ads-H+}(j)$ were used for dehydrogenation.) Figure 6 shows plots of $\Delta H_{int}^{\ddagger}$ vs ΔH_{ads-H+} and $\Delta S_{int}^{\ddagger}$ vs ΔS_{ads-H+}. It can be seen that the changes in $\Delta H_{int}^{\ddagger}$ and $\Delta S_{int}^{\ddagger}$ with respect to ΔH_{ads-H+} and ΔS_{ads-H+} mirror the changes in ΔH_{app} and ΔS_{app} seen in Figure 5 and, therefore, contribute significantly to changes in ΔH_{app} and ΔS_{app} with confinement. These conclusions differ from the previous reports[16,18−24] that intrinsic activation parameters are independent of zeolite structure. Moreover, the variation in $\Delta H_{int}^{\ddagger}$ for terminal cracking and dehydrogenation seen in Figure 6 is unlikely to be caused by variation in acid strength, which these studies have suggested affects the value of $\Delta H_{int}^{\ddagger}$. As noted in the Introduction, the heat of protonation for NH$_3$ calculated by Derouane et al.[26] is nearly the same for MFI, FER, and MOR. In addition, if acidity is a function of confinement, it seems unlikely that the activation energy for central cracking

would not vary with ΔS_{ads-H+}, and there is no obvious explanation based on acidity alone for why values of $\Delta S_{int}^{\ddagger}$ would change in the manner observed in Figure 6. Therefore, we conclude that the changes observed in intrinsic activation parameters are a consequence of changes in confinement, as discussed further in section 4.4.2.

Given that the changes in $\Delta H_{int}^{\ddagger}$ and $\Delta S_{int}^{\ddagger}$ with confinement in Figure 6 are well behaved within the 10-MR straight channel group, it is appropriate to discuss reasons for why $\Delta H_{int}^{\ddagger}$ and $\Delta S_{int}^{\ddagger}$ for SFV do not adhere to the same trends, since ~87%[33] of the 10-MR and 12-MR channels of SFV are 10-MR. Recalling that ΔH_{ads-H+} and ΔS_{ads-H+} have been calculated by assuming a random distribution of Al, it can be assumed that if the Al for the two samples of SFV investigated (see Table 1) is in fact located mostly in the 10-MR, that values of ΔH_{ads-H+} and ΔS_{ads-H+} would be closer to those for TON, which consists only of 10-MR channels. This possibility does not seem unreasonable given that ~70%[33] of the total pore volume of SFV is located in 10-MR channels. By examining Figure 6 it can be seen that if $\Delta H_{int}^{\ddagger}$ and $\Delta S_{int}^{\ddagger}$ for SFV appeared at values of ΔH_{ads-H+} and ΔS_{ads-H+} closer to those for TON, $\Delta H_{int}^{\ddagger}$ and $\Delta S_{int}^{\ddagger}$ for SFV would be more consistent with the overall trends observed for zeolites having 10-MR straight channels. This assessment takes into account the increases in $\Delta H_{int}^{\ddagger}$ and $\Delta S_{int}^{\ddagger}$ that would accompany the changes in ΔH_{ads-H+} and ΔS_{ads-H+} (based on eqs 6 and 7). These observations suggest that the distribution of Al within the SFV samples investigated is skewed toward the 10-MR channels.

4.4.2. Dependence of Rate Coefficients on Zeolite Structure and on Activation Parameters. The changes in intrinsic and apparent activation parameters with respect to confinement discussed above determine how confinement affects rate coefficients, which depend exponentially on these parameters (eqs 4 and 5). Based on the earlier observations in the literature for *n*-hexane cracking and dehydrogenation over MFI, MOR, and FAU,[19,22] k_{app} would be expected to increase with increasing confinement as a result of increases in K_{ads-H+},
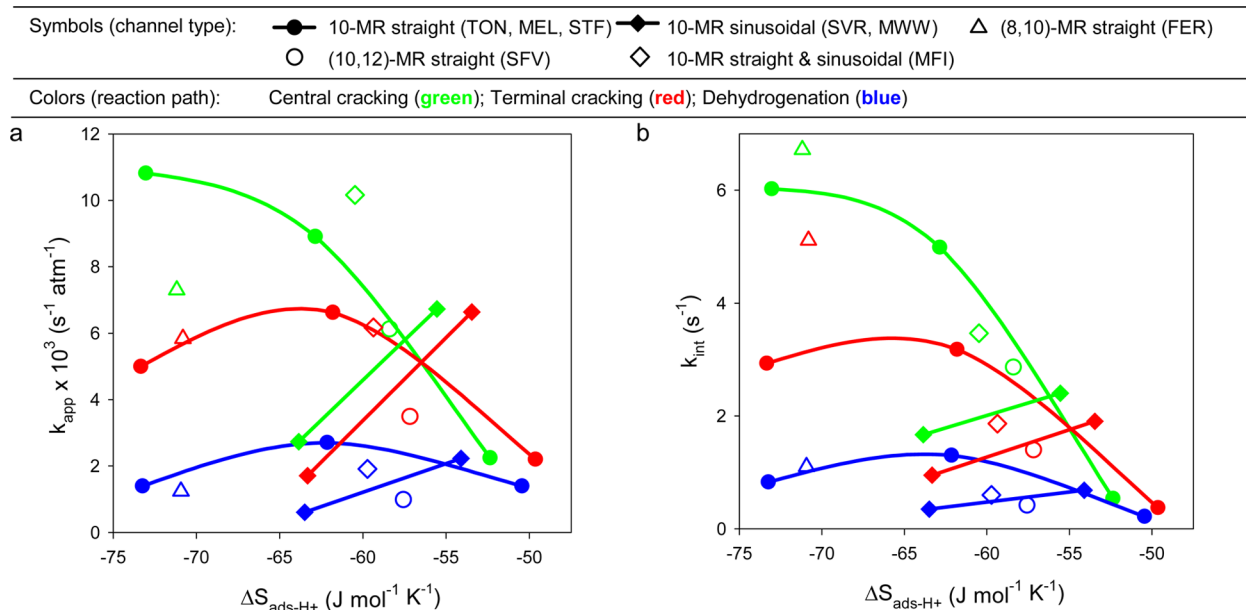
Figure 8. Plots of (a) apparent (measured) first-order rate coefficient, and (b) intrinsic rate coefficient calculated using eq 4 and activation parameters shown in Figure 6, for *n*-butane monomolecular reactions vs entropy of adsorption at 773 K (determined using CBMC simulations). Representative 95% confidence intervals for rate coefficients are ±8% for cracking and ±9% for dehydrogenation.

while k_{int} would be expected to remain constant or at least not dependent on pore size. Figure 7a and 7b show plots of k_{app} vs K_{ads-H+} and k_{app} vs k_{int}. The values of k_{int} were calculated using eq 4 and the intrinsic activation parameters presented in Figure 6. Figure 7 shows that, by contrast to the reports for *n*-hexane noted above, k_{app} for zeolites with 10-MR straight channels increases as K_{ads-H+} decreases and increases as k_{int} increases. For zeolites with sinusoidal channels, k_{app} increases with increasing K_{ads-H+}, while k_{int} is nearly constant, and the dependences of k_{app} on both K_{ads-H+} and k_{int} are therefore similar to what has been reported for *n*-hexane. Thus, k_{int} affects k_{app} more strongly than does K_{ads-H+} for the zeolites with 10-MR straight channels, while K_{ads-H+} dominates the value of k_{app} for the zeolites with sinusoidal channels.

To understand the relationship of k_{app} and k_{int} to confinement, these quantities are plotted vs ΔS_{ads-H+} in Figure 8a and 8b. It can be seen that k_{app} generally increases with increasing confinement (i.e., as ΔS_{ads-H+} becomes more negative) for 10-MR straight channels, albeit irregularly for terminal cracking and dehydrogenation, and that k_{app} decreases with increasing confinement for 10-MR sinusoidal channels. The irregular changes in k_{app} for the former set of zeolites are a consequence of the fact that k_{int} and K_{ads-H+} change in opposite directions (Figure 3), since k_{app} is proportional to both k_{int} and K_{ads-H+}. It is interesting that, although k_{app} for the sinusoidal channel group reflects predominantly variation in K_{ads-H+} (similar to the finding for *n*-hexane), the dependences of k_{app} and K_{ads-H+} on *confinement* are the reverse of those reported for hexane; both parameters decrease with increasing confinement because the decrease in ΔS_{ads-H+} causes K_{ads-H+} to decrease. For the zeolites with 10-MR straight channels, k_{app} increases with increasing confinement, but due to an increase in k_{int} and not due to an increase in K_{ads-H+}. These results demonstrate that an increase in confinement can affect the value of k_{int} and does not in general cause k_{app} or K_{ads-H+} to increase.

We next interpret the physical reasons for the observed variation of intrinsic rate coefficients with confinement and

zeolite structure seen in Figure 8b. We begin by recalling that, as can be seen in Figure 6, for a given channel type $\Delta H_{int}^{\ddagger}$ and $\Delta S_{int}^{\ddagger}$ for terminal cracking and dehydrogenation decrease as confinement increases, while for central cracking $\Delta S_{int}^{\ddagger}$ increases and $\Delta H_{int}^{\ddagger}$ is nearly invariant. By comparing the change in k_{int} with respect to ΔS_{ads-H+} for central cracking to the changes in $\Delta S_{int}^{\ddagger}$ and $\Delta H_{int}^{\ddagger}$, it can be seen that the increase in k_{int} for zeolites with 10-MR straight channels is driven primarily by an increase in $\Delta S_{int}^{\ddagger}$. A similar increase in k_{int} is not observed for the sinusoidal channel group because $\Delta H_{int}^{\ddagger}$ also increases slightly with confinement. The increase in $\Delta S_{int}^{\ddagger}$ for central cracking with increasing confinement appears to be counterintuitive, but can be rationalized by analyzing the contributions of the reactant state entropy (S_{react}) and transition-state entropy ($S^{\ddagger}$) to $\Delta S_{int}^{\ddagger}$, equal to $S^{\ddagger} - S_{react}$.

Sharada et al.[15] have shown that the transition state for C−C bond cracking in MFI occurs early along the reaction coordinate. In addition, this transition state interacts closely with the oxygen atoms bonded to the Al atom. The transition state is, therefore, more restricted in movement than is the reactant state. This assessment is supported by consistently negative values of $\Delta S_{int}^{\ddagger}$ for central cracking observed in Figure 6b. For such a transition state, the main modes contributing to $S^{\ddagger}$ are vibrational because the product fragments have not been formed and because the transition state is tightly bound to the active site. Because of the close interaction of the transition state with the framework and the lack of translational or rotational motion, it can be inferred that the spaciousness of the environment surrounding the active site has much less influence on the motion of the transition state than on the motion of the reactant state. If this hypothesis is true, then differences in $\Delta S_{int}^{\ddagger}$ between zeolite structures should be roughly equal to differences in S_{react}, and therefore equal to differences in ΔS_{ads-H+}. Indeed, it can be seen from Figure 6b that differences in $\Delta S_{int}^{\ddagger}$ within a given channel group are similar to the differences in ΔS_{ads-H+}. These observations support the proposal that the transition state for central cracking is early
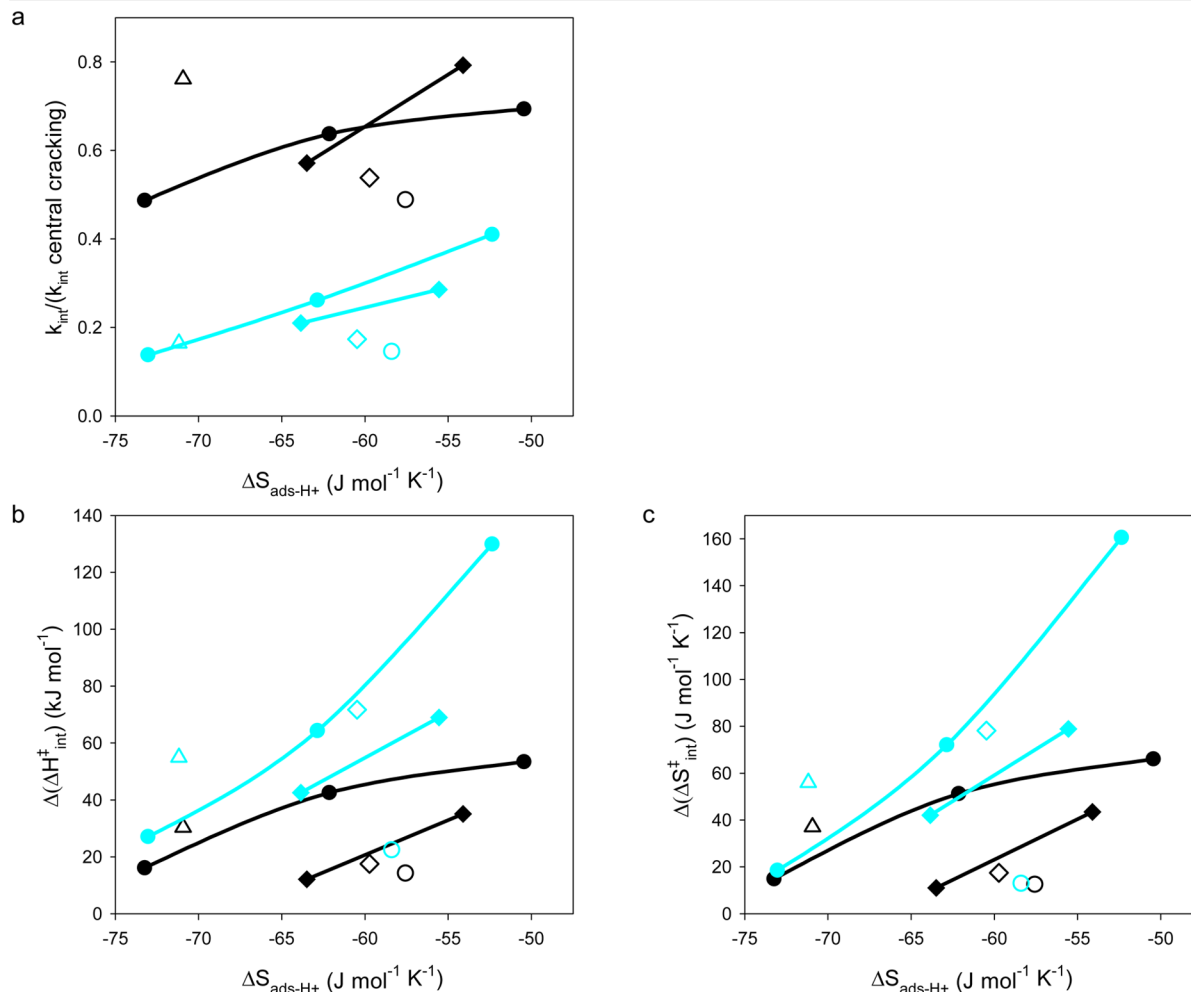
Figure 9. (a) Ratios of intrinsic rate coefficient for *n*-butane dehydrogenation relative to central cracking and for terminal cracking relative to central cracking, and corresponding differences between intrinsic activation (b) enthalpies, and (c) entropies, vs entropy of adsorption at 773 K determined from CBMC simulations. Representative 95% confidence intervals for rate ratios are ±7% for terminal cracking and ±8% for dehydrogenation. Confidence intervals for $\Delta(\Delta H_{int}^{\ddagger})$ and $\Delta(\Delta S_{int}^{\ddagger})$ are ±9 kJ mol^{-1} and ±12 J mol^{-1} K^{-1} for terminal cracking, and ±10 kJ mol^{-1} and ±14 J mol^{-1} K^{-1} for dehydrogenation.

and suggest that the increase in $\Delta S_{int}^{\ddagger}$ (equal to $S^{\ddagger} - S_{react}$) with confinement arises primarily from a decrease in S_{react}.

Stated differently, alkanes in a reactant state within a zeolite that has a very confining structure (e.g., TON) are already very confined and, hence, lose relatively little translational and rotational entropy upon movement from the reactant state to the tightly bound transition state for central cracking. By contrast, reactant-state alkanes within a structure comprised mostly of cages (e.g., STF) have more translational and rotational freedom and lose more entropy upon forming the transition state, provided that the structure of this transition state is similar for the two zeolites. This interpretation is consistent with recent theoretical work reported by Bučko and Hafner.[17] These authors found that for propane adsorbed within MOR, cracking occurs at a faster rate within the 8-MR pockets relative to the 12-MR channels because the alkane is already highly confined when adsorbed near a proton within the 8-MR pocket. As a result, the entropic cost of protonation is

lower for the 8-MR vs the 12-MR, and k_{int} is commensurately larger for the 8-MR.

We next discuss the influence of confinement on the intrinsic rate coefficients for terminal cracking and dehydrogenation. It can be seen from Figure 8b that k_{int} for terminal cracking and dehydrogenation is similar for zeolites with 10-MR sinusoidal channels. For zeolites having 10-MR straight channels, k_{int} is smallest for the least confining zeolite (STF) and increases nonmonotonically as ΔS_{ads-H+} decreases. By comparing these changes in k_{int} to those observed for $\Delta H_{int}^{\ddagger}$ and $\Delta S_{int}^{\ddagger}$ in Figure 6 it can be seen that the irregular changes in k_{int} are driven by simultaneous decreases in $\Delta H_{int}^{\ddagger}$ and $\Delta S_{int}^{\ddagger}$ as confinement increases. Decreases in one quantity thus partly compensate for decreases in the other in determining $\Delta G_{int}^{\ddagger}$.

The fact that $\Delta H_{int}^{\ddagger}$ and $\Delta S_{int}^{\ddagger}$ for terminal cracking and dehydrogenation appear to increase, rather than remain similar or decrease with decreasing confinement as was observed for central cracking, can be rationalized by assuming that the transition states of the former reactions are later and more

closely resemble product fragments, or interact more weakly with the active site relative to central cracking. Such transition states are expected to have similar or even greater freedom of movement relative to reactant-state *n*-butane. Consistent with this proposal, Figure 6 shows that values of $\Delta S_{int}^{\ddagger}$ for terminal cracking and dehydrogenation are usually ~0 or positive, suggesting that transition states for these reactions involve the formation of rotational or translational entropy. Such motion is only possible if sufficient space surrounds the active site; thus, $\Delta S_{int}^{\ddagger}$ is, in general, more positive for less confining zeolites. In addition, the observation that $\Delta S_{int}^{\ddagger}$ for dehydrogenation is nearly always greater than $\Delta S_{int}^{\ddagger}$ for terminal cracking is consistent with theoretical calculations,[15] which show that the transition state for dehydrogenation most strongly resembles the products.

4.4.3. Dependence of Selectivity on Zeolite Structure and on Relative Activation Parameters. The above discussion shows that the effects of zeolite structure on $\Delta H_{int}^{\ddagger}$ and $\Delta S_{int}^{\ddagger}$ for *n*-butane cracking and dehydrogenation result in systematic dependences of intrinsic rate coefficients on confinement. Since confinement affects k_{int} differently for different reaction pathways (see Figure 8b), confinement must also affect selectivity, which is discussed next. Plots of the ratios of k_{int} for terminal cracking relative to central cracking, and k_{int} for dehydrogenation relative to central cracking, versus ΔS_{ads-H+} are presented in Figure 9a. It can be seen that, for a given channel type, as confinement increases, the selectivities to terminal cracking and—more strongly—to dehydrogenation decrease relative to central cracking. To interpret how the zeolite structure influences these trends, we note that according to eq 4 the ratios of k_{int} are exponentially dependent on the differences in $\Delta H_{int}^{\ddagger}$ and $\Delta S_{int}^{\ddagger}$ for one reaction path relative to another ($\Delta(\Delta H_{int}^{\ddagger})$ and $\Delta(\Delta S_{int}^{\ddagger})$).

Figure 9b and 9c show plots of $\Delta(\Delta H_{int}^{\ddagger})$ and $\Delta(\Delta S_{int}^{\ddagger})$ for dehydrogenation and terminal cracking relative to central cracking, versus ΔS_{ads-H+}. From a comparison of trends in $\Delta(\Delta H_{int}^{\ddagger})$ and $\Delta(\Delta S_{int}^{\ddagger})$ with respect to confinement to those seen for the selectivity ratios in Figure 9a, it is evident that the main factor driving the differences in selectivity among zeolites within a given channel category is $\Delta(\Delta S_{int}^{\ddagger})$. For example, for zeolites with 10-MR straight and 10-MR sinusoidal channels, the ratio of dehydrogenation relative to cracking decreases as $\Delta(\Delta H_{int}^{\ddagger})$ decreases, and the same is true for terminal cracking relative to central cracking. Therefore, the decreasing selectivity to dehydrogenation and terminal cracking with increasing confinement must arise from the offsetting effects of decreases in $\Delta(\Delta S_{int}^{\ddagger})$. Considering the decrease in selectivity to the higher energy cracking pathway that occurs with increasing confinement (observable in Figure 9), it is conceivable that there is also a concurrent decrease in selectivity to methyl versus methylene dehydrogenation. Such a change in the selectivity of the dehydrogenation cannot be discerned experimentally because the linear butene isomers (which are primary products of dehydrogenation) isomerize rapidly. However, the proposed change in selectivity would contribute to a decrease in the observed values of $\Delta(\Delta H_{int}^{\ddagger})$ and $\Delta H_{int}^{\ddagger}$ (in addition to effects of confinement on $\Delta H_{int}^{\ddagger}$ for individual dehydrogenation pathways), because the activation energy for methyl C—H dehydrogenation significantly exceeds that for methylene dehydrogenation (by ~60 kJ mol^{-1} for MFI).[15]

We note that, according to Gounder and Iglesia,[23] the plots shown in Figure 9b and 9c should exhibit horizontal lines intersecting the vertical axes at the differences in the enthalpy

or entropy of gas phase alkane molecules protonated at the corresponding C—C or C—H bonds. While protonation entropy data are not available, the protonation enthalpies (or proton affinities) of C—H and terminal C—C bonds relative to central C—C bonds are, respectively, ~60 and ~19 kJ mol^{-1}.[23] Several data points of Figure 9b—including, notably, those for MFI and FER, zeolites that were investigated by Gounder and Iglesia—lie near these values, but in general $\Delta(\Delta H_{int}^{\ddagger})$ and $\Delta(\Delta S_{int}^{\ddagger})$ decrease as confinement increases. This result is consistent with the observation of smaller differences between activation energies (calculated using QM/MM)[15] for the monomolecular cracking and dehydrogenation of *n*-butane at sinusoidal channels versus at intersections within MFI.

To understand why the difference in proton affinity (ΔPA) does not always approximate $\Delta(\Delta H_{int}^{\ddagger})$ it is necessary to understand the assumptions that must hold in order for this equality to be true.[16,23] Specifically, the approximation requires the formation of an ion pair at the transition state with full transfer of the proton to the alkane. The structure of the alkane at the transition state must be very similar to that of the gas-phase alkane protonated at the C—C or C—H bond to be cleaved. In addition, the interaction energy of the protonated alkane with the deprotonated active site must be identical for different transition states. A thermochemical cycle[16,23] can be used to show that under these circumstances $\Delta(\Delta H_{app})$ ($\approx \Delta(\Delta H_{int}^{\ddagger})$) = ΔPA. Consistent with this reasoning, DFT calculations[68,69] show that when a zeolite proton is completely transferred to a small Lewis base upon adsorption from the gas phase onto an acid site, the difference in the energy of adsorption $\Delta(\Delta U_{ads-H+})$ between different adsorbates—analogous to $\Delta(\Delta H_{app})$ for transition states—is very similar to ΔPA. The calculations also show that when an ion pair is *not* formed (as for weak bases), then $\Delta(\Delta U_{ads-H+}) \neq \Delta$PA. It is noted that these calculations[68,69] do not take into account the effects of dispersion forces on ΔU_{ads-H+}; however, as discussed by the authors, dispersion should contribute negligibly to ΔU_{ads-H+} for the small bases investigated.

Therefore, we next examine whether it can be reasonably assumed that ion pairs, and transition states similar in structure to gas-phase carbonium ions, are formed at transition states in monomolecular cracking or dehydrogenation. In previous theoretical work from our group, significant structural differences were observed between the transition states for cracking and dehydrogenation of *n*-butane in H-MFI.[15] For example, in the transition state for dehydrogenation, product fragments are nearly formed and the zeolitic proton is nearly regenerated, which differs from the description of an ion pair interaction between a deprotonated zeolite and a protonated alkane. By contrast, the central cracking transition state more qualitatively resembles a protonated alkane in structure. These qualitative observations suggest that ion pairs similar in structure to carbonium ions are not formed exclusively at cracking and dehydrogenation transition states and that, therefore, it should not be expected that $\Delta(\Delta H_{app})$ ($\approx \Delta(\Delta H_{int}^{\ddagger})$) is generally equal to ΔPA. Consistent with this proposal, differences in activation energies among monomolecular reactions of *n*-butane, determined using QM/MM calculations,[15] differ from the values of ΔPA mentioned above and cited by Gounder and Iglesia[23] (see ref 15, Table 2). It can, however, be seen from Figure 9 and ref 23 that the values of ΔPA appear to give reasonable first approximations for $\Delta(\Delta H_{int}^{\ddagger})$ for some zeolites of low and intermediate confinement. Although our analysis and the trends observable in Figure 9 indicate that confinement
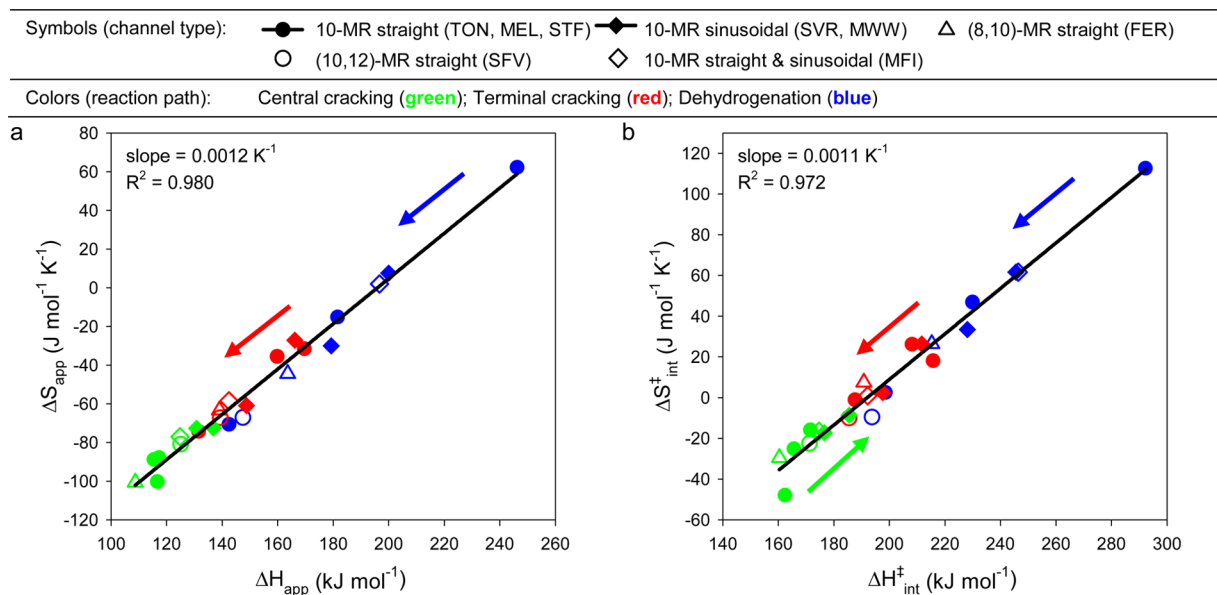
Figure 10. Plots of (a) apparent activation entropy vs activation enthalpy values from Figure 5, and (b) intrinsic activation entropy vs activation enthalpy values from Figure 6 for *n*-butane monomolecular reactions at 773 K. The slopes and R^2 values of linear fits of the data are included on the plots. Representative 95% confidence intervals for activation enthalpies and entropies are ± 7 kJ mol^{-1} and ± 9 J mol^{-1} K^{-1} for cracking, and ± 8 kJ mol^{-1} and ± 11 J mol^{-1} K^{-1} for dehydrogenation. Arrows indicate the general direction of increasing confinement (arrow omitted from (a) for central cracking because ΔH_{app} and ΔS_{app} do not depend on confinement).

affects the relative activation parameters, it can be reasonably assumed that in some cases the assumptions that must be satisfied in order for $\Delta(\Delta H_{int}^{\ddagger})$ to equal ΔPA are valid, or that breakdowns in these assumptions tend to offset one another, leading (in either case) to the observation that $\Delta(\Delta H_{int}^{\ddagger}) = \Delta PA$.

4.4.4. Observed Correlation between Entropy and Enthalpy of Activation. From the analysis presented in section 4.4.1 it is apparent that changes in the activation enthalpy and entropy tend to occur in the same direction with respect to changes in confinement and are, therefore, correlated. A positive linear correlation between ΔH_{app} and ΔS_{app} would be consistent with the linear Constable plot reported by van Bokhoven et al.[19] for the total rate of *n*-hexane cracking and dehydrogenation, and with a plot of ΔS_{app} vs ΔH_{app} reported in more recent work[70] for C3–C8 alkanes that was also found to be linear. Correlation between $\Delta H_{int}^{\ddagger}$ and $\Delta S_{int}^{\ddagger}$ would not be expected based on reports in the literature (noted in the Introduction) that these quantities are structure-insensitive. Before examining these correlations, however, it is important to address the statistical treatment of uncertainties in ΔH_{app} and ΔS_{app}, because apparent correlations between these parameters can arise from correlations of errors in ΔH_{app} and ΔS_{app}[71,72] as well as from underlying physical phenomena.[73–77] As described in the Supporting Information (section S.5), the proper way to determine whether an apparent correlation between ΔH_{app} and ΔS_{app} is a statistical artifact is to first determine the 95% confidence regions in the ΔH_{app}–ΔS_{app} plane for each set of values for ΔH_{app} and ΔS_{app}. Correlation beyond these regions is statistically significant.

Figure 10a shows a plot of ΔS_{app} vs ΔH_{app}. It can be seen that there is a strong, positive correlation between ΔS_{app} and ΔH_{app} that extends well beyond the uncertainties in individual data points (given in the caption) and is, therefore, statistically significant. The high R^2 value for the linear fit of these data, shown by the solid line, causes the values of k_{app} to not vary by

many orders of magnitude among zeolites and reaction pathways (see Figure 8a). Because of the correlation, the values of ΔG_{app} (equal to $\Delta H_{app} - T\Delta S_{app}$) are similar and the effect of a change in ΔH_{app} on ΔG_{app} and k_{app} is partly offset by a similar change in $T\Delta S_{app}$. Arrows are shown on the plot to indicate the direction in which confinement tends to increase for each reaction pathway. Within a given channel group, the distance of each data point along this line (the point of intersection of a line drawn from the data point orthogonal to the fitted line) is correlated with the values of ΔS_{ads-H+} and ΔH_{ads-H+} in Figure 5. Consistent with the differing effects of confinement on activation parameters for terminal cracking and dehydrogenation relative to central cracking (see Figures 5 and 6), the arrows for dehydrogenation and terminal cracking point in the opposite direction to those for central cracking.

We note that some correlation between ΔS_{app} and ΔH_{app} is expected based on eqs 6 and 7, since ΔS_{ads-H+} and ΔH_{ads-H+} are themselves correlated (see Figure 4). However, it can be seen from a plot of $\Delta S_{int}^{\ddagger}$ vs $\Delta H_{int}^{\ddagger}$ in Figure 10b that correlation between $\Delta S_{int}^{\ddagger}$ and $\Delta H_{int}^{\ddagger}$ is the main driver of the correlation observed between ΔS_{app} and ΔH_{app}; the slope of a linear fit of the data in Figure 10b is 0.0011 K^{-1}, which is closer to the slope of ΔS_{app} vs ΔH_{app} in Figure 10a (0.0012 K^{-1}) than is the slope of ΔS_{ads-H+} vs ΔH_{ads-H+} shown in Figure 4 (0.0020 K^{-1}). This finding is consistent with the observation discussed in section 4.4.1 that changes in $\Delta S_{int}^{\ddagger}$ and $\Delta H_{int}^{\ddagger}$ with confinement influence the values of ΔS_{app} and ΔH_{app} more strongly than do changes in ΔS_{ads-H+} and ΔH_{ads-H+}. We also note that the slope and intercept of the fitted lines shown in Figure 10 are not useful for predicting trends in k_{app} or k_{int} with respect to confinement (e.g., distance along the fitted line) because the data points do not fall exactly on the fitted lines. Ryde[77] has used theoretical methods to demonstrate that correlation between entropy and enthalpy is a general rule for several types of intermolecular interactions (e.g., electrostatic, dispersive), yet perfect correlation arises only when a single variable and
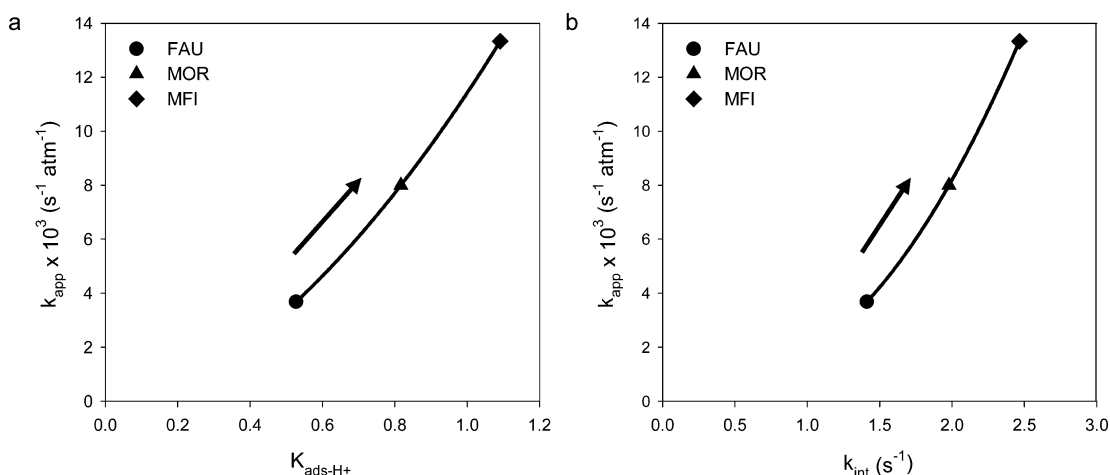
Figure 11. Plots of the apparent (measured) rate coefficient for the total rate of monomolecular consumption (per bond) of *n*-hexane over MFI, MOR, and FAU at 773 K[19] vs (a) adsorption equilibrium constant determined using CBMC simulations and (b) intrinsic rate coefficient determined using eq 4 and intrinsic activation parameters calculated using eqs 6 and 7. Lines through the data points are included to guide the eye. Arrows indicate the direction of increasing confinement.

interaction type change within a homologous series. Table 2 shows that several topological descriptors differ among the zeolites investigated in this study.

We next rationalize qualitatively the reasons for the positive correlation between $\Delta H_{int}^{\ddagger}$ and $\Delta S_{int}^{\ddagger}$ seen in Figure 10b. Given that increases in $\Delta S_{int}^{\ddagger}$ are driven primarily by access to more rotational and translational modes, as discussed above, it can be assumed that higher values of $\Delta S_{int}^{\ddagger}$ correspond to transition states for which there is greater separation of charge and weaker interactions of the transition state with the O atoms bonded to the Al atom. This would result in enthalpic destabilization and would increase $\Delta H_{int}^{\ddagger}$. This interpretation is in qualitative agreement with that proposed by Dunitz,[78] who used a statistical mechanical model to demonstrate that enthalpy–entropy compensation is a general phenomenon for weak intermolecular interactions, and is also consistent with explanations for compensation between $\Delta S_{ads\text{-}H+}$ and $\Delta H_{ads\text{-}H+}$ observed for alkane adsorption in zeolites. The latter has been rationalized based on the observation that larger magnitudes of $\Delta H_{ads\text{-}H+}$ generally require closer interaction of alkane molecules with the zeolite and, therefore, a greater loss in entropy.[79]

In addition, Conner[80] has proposed an explanation for entropy–enthalpy compensation in catalysis that is consistent with the dependences of $\Delta H_{int}^{\ddagger}$ and $\Delta S_{int}^{\ddagger}$ on confinement observed in the present work. He argues that increased vibrational and rotational coupling between a surface and a transition-state complex is associated with a lower energy of the transition state relative to the reactant state and lowers the degeneracy of individual energy levels. This leads to fewer accessible energy states and lowers the value of $\Delta S_{int}^{\ddagger}$. Using these arguments, higher values of $\Delta H_{int}^{\ddagger}$ would be expected for less confined active sites, for which less coupling would be expected between the transition state and the zeolite, provided the transition state is late and resembles freely moving product fragments. Consistent with this picture, $\Delta H_{int}^{\ddagger}$ and $\Delta S_{int}^{\ddagger}$ for terminal cracking and dehydrogenation, but not for central cracking, generally increase with decreasing confinement in Figure 6, with the exception of SFV for the reasons postulated in section 4.4.1.

4.5. Reexamination of the Influence of Zeolite Structure on Kinetics of *n*-Hexane Cracking and Dehydrogenation. Having shown how the kinetics of *n*-butane cracking and dehydrogenation depend on zeolite structure and confinement for the zeolites listed in Table 2, we now return to the previous studies of monomolecular *n*-hexane cracking[19,22] discussed in the Introduction. As noted, Ramachandran et al.[22] concluded that k_{app} for the total rate of monomolecular *n*-hexane consumption (reported by van Bokhoven et al.)[19] increased with increasing confinement (i.e., in moving from FAU to MOR to MFI) because of an increase in the heat of adsorption and the adsorption equilibrium constant, and that intrinsic kinetics were structure-insensitive. This conclusion was based on the observation of similar slopes for a plot of the entropy of adsorption vs the enthalpy of adsorption and for a Constable plot reported by van Bokhoven et al.[19] However, these conclusions were reached using adsorption data corresponding to nonspecific adsorption, and not to a reactant state at Brønsted protons, and measured near ambient temperature. Therefore, differences in intrinsic kinetic parameters among zeolites may have been missed because of a lack of values of $\Delta H_{ads\text{-}H+}$ and $\Delta S_{ads\text{-}H+}$ for specific adsorption or at temperatures of the rate measurements. Below, intrinsic kinetic parameters are obtained and analyzed from the data reported by van Bokhoven et al.[19] using values of $\Delta H_{ads\text{-}H+}$ and $\Delta S_{ads\text{-}H+}$ determined from CBMC simulations as described in section 3.

Values of $\Delta S_{int}^{\ddagger}$ and $\Delta H_{int}^{\ddagger}$ were calculated by subtracting $\Delta H_{ads\text{-}H+}$ and $\Delta S_{ads\text{-}H+}$ at 773 K (included in the Supporting Information, section S.6) from ΔH_{app} and ΔS_{app}, which were determined using eq 5 and values of k_{app} (normalized to the number of bonds) and E_{app} taken from ref 19. The adsorption equilibrium constant, $K_{ads\text{-}H+}$, and intrinsic rate coefficient, k_{int}, were then determined using eqs 3 and 4 to investigate the dependence of k_{app} on each parameter. Details of these calculations, and topological descriptors for the zeolites, are included in section S.6. Plots of k_{app} vs $K_{ads\text{-}H+}$ and k_{app} vs k_{int} are presented in Figure 11a and 11b. Arrows included on the plots indicate the direction of increasing magnitudes for $\Delta H_{ads\text{-}H+}$ and $\Delta S_{ads\text{-}H+}$ and, therefore, increasing confinement. It can be seen that k_{app} increases as both $K_{ads\text{-}H+}$ and k_{int} increase, indicating

that changes in k_{app} are not dominated by changes in either parameter and that all three parameters increase with increasing confinement. Thus, K_{ads-H+} must be controlled by the value of ΔH_{ads-H+}. These observations differ from those for n-butane cracking and dehydrogenation over the zeolites listed in Table 2, for which k_{app} and k_{int} depended on confinement differently for zeolites having different channel topologies (see Figure 8), and for which K_{ads-H+} was controlled by the value of ΔS_{ads-H+} (see Figure 3) and decreased with increasing confinement. As shown in the Supporting Information (section S.6), the different observations for adsorption thermodynamics of n-butane and n-hexane are a consequence of the different sets of zeolites used for each alkane, and not of alkane size.

A plot of $\Delta S_{int}^{\ddagger}$ vs $\Delta H_{int}^{\ddagger}$ is shown in Figure 12. It can be seen that $\Delta S_{int}^{\ddagger}$ and $\Delta H_{int}^{\ddagger}$ are correlated and that each decreases as
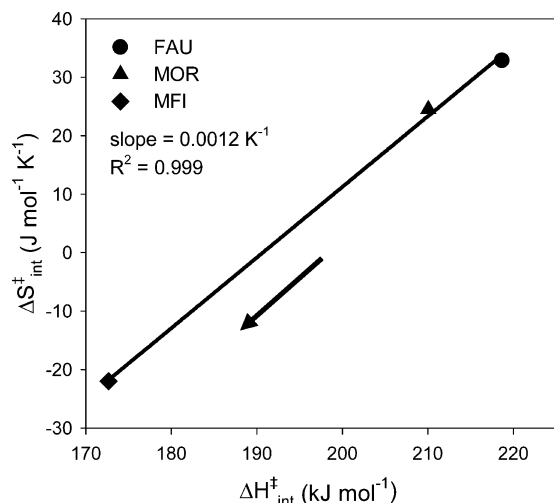
Figure 12. Plot of intrinsic activation entropy vs intrinsic activation enthalpy for monomolecular consumption of n-hexane over MFI, MOR, and FAU, determined using eqs 6 and 7, adsorption data from CBMC simulations, and measured rate data taken from ref 19. The slope and R^2 values of a linear fit are included on the plot. The arrow indicates the direction of increasing confinement.

confinement increases (in the direction indicated by the arrow). Thus, $\Delta S_{int}^{\ddagger}$ and $\Delta H_{int}^{\ddagger}$ for the total rate of n-hexane monomolecular consumption depend on confinement in a qualitatively similar way to $\Delta S_{int}^{\ddagger}$ and $\Delta H_{int}^{\ddagger}$ for terminal cracking and dehydrogenation of n-butane (Figure 10b). This observation can be partly attributed to changes in the selectivity to activation of C–H and C–C bonds with respect to confinement, seen in Figure 9 for n-butane, but is also consistent with changes in intrinsic activation parameters for individual reaction pathways. By contrast, the relationship of k_{int} to confinement is more complex because the correlation of $\Delta S_{int}^{\ddagger}$ and $\Delta H_{int}^{\ddagger}$. The similarity of the slope of the linear fit of the data in Figure 12 ($\sim$0.0012 K^{-1}) to that of the Constable plot of ref 19 and to the slope of a plot of ΔS_{ads-H+} vs ΔH_{ads-H+} included in the Supporting Information (section S.6) also demonstrates that the slope of the Constable plot reflects correlation of the adsorption parameters, as proposed by Ramachandran et al.,[22] as well as correlation of intrinsic activation parameters. The above results demonstrate that $\Delta S_{int}^{\ddagger}$ and $\Delta H_{int}^{\ddagger}$ for n-hexane monomolecular consumption over MFI, MOR, and FAU vary with confinement in a similar manner as do $\Delta S_{int}^{\ddagger}$ and $\Delta H_{int}^{\ddagger}$ for n-butane cracking and dehydrogenation over the eight zeolites listed in Table 2. However, the

dependences of K_{ads-H+} and k_{int} on structural confinement, and the relative contribution of each parameter to k_{app} in general, depend on the zeolites chosen for study.

5. CONCLUSIONS

We have systematically characterized the effects of zeolite structure and confinement on adsorption thermodynamics and intrinsic kinetics of n-butane monomolecular cracking and dehydrogenation in acidic zeolites differing primarily in the size and abundance of cavities and in channel topology. We have modified our previous method[27] for determining enthalpies and entropies of adsorption of gas-phase alkanes onto Brønsted protons (ΔH_{ads-H+} and ΔS_{ads-H+}) using Monte Carlo simulations. Specifically, we have reduced computational cost by employing Widom particle insertions in combination with domain decomposition, and we have improved the parameters and transferability of the Lennard–Jones force field used to model the interaction of alkanes with zeolite acid sites.

We find that the adsorption equilibrium constant (K_{ads-H+}) at 773 K depends primarily on the value of ΔS_{ads-H+}, rather than on ΔH_{ads-H+}, and that K_{ads-H+} therefore tends to be lower for adsorption in more confining zeolites. The value of K_{ads-H+} largely determines the measured rate coefficient (k_{app}) for zeolites having 10-MR sinusoidal channels, while the intrinsic rate coefficient (k_{int}) determines the value of k_{app} for zeolites having 10-MR straight channels. These results contrast previous reports that K_{ads-H+} is determined by ΔH_{ads-H+} and is in general the cause of differences in k_{app} for n-alkane cracking over MFI, MOR, BEA, and FAU.[18−21]

We also find that k_{int} tends to increase with increasing confinement (i.e., as ΔS_{ads-H+}—used as a proxy for confinement—becomes more negative) for zeolites with 10-MR straight channels and is similar for zeolites with 10-MR sinusoidal channels. For central cracking, an early transition state, this increase is strongest and is driven by an increase in the intrinsic activation entropy, $\Delta S_{int}^{\ddagger}$. For dehydrogenation and—more strongly—for terminal cracking, k_{int} increases with increasing confinement because the intrinsic enthalpy of activation, $\Delta H_{int}^{\ddagger}$, decreases. The decrease in $\Delta H_{int}^{\ddagger}$, however, is accompanied by a decrease in $\Delta S_{int}^{\ddagger}$ that causes the changes in k_{int} to be nonmonotonic and the selectivities to terminal cracking and dehydrogenation to decrease relative to central cracking. The variation in $\Delta H_{int}^{\ddagger}$ with confinement is unlikely to be caused by changes in acidity, because $\Delta H_{int}^{\ddagger}$ for central cracking does not change with confinement, and acidity is not expected to cause large changes in $\Delta S_{int}^{\ddagger}$.

The observation of structure-dependent differences between $\Delta S_{int}^{\ddagger}$ and $\Delta H_{int}^{\ddagger}$ for different reaction paths shows that these differences are not always equal to differences in the gas-phase protonation enthalpy and entropy of C–C and C–H bonds, because transition states do not always resemble ion pairs consisting of the deprotonated zeolite and a gas-phase carbonium ion. The concurrent decreases in both $\Delta S_{int}^{\ddagger}$ and $\Delta H_{int}^{\ddagger}$ for terminal cracking and dehydrogenation with increasing confinement, as well as positive values observed for $\Delta S_{int}^{\ddagger}$, are consistent with transition states for these reactions that are weakly bound and involve rotations and translations of product fragments.

Finally, using simulated values of ΔH_{ads-H+} and ΔS_{ads-H+}, we have extracted values of $\Delta S_{int}^{\ddagger}$ and $\Delta H_{int}^{\ddagger}$ from previously reported experimental data for n-hexane monomolecular conversion over MFI, MOR, and FAU.[19] We find that, similar to n-butane terminal cracking and dehydrogenation over the

zeolites employed in the present work, $\Delta S_{int}^{\ddagger}$ and $\Delta H_{int}^{\ddagger}$ for the overall rate of n-hexane consumption decrease with increasing confinement. This result differs from the conclusions given in the literature that $\Delta S_{int}^{\ddagger}$ [19,22,23] and $\Delta H_{int}^{\ddagger}$ [16,18–22] are structure-independent. We find that both K_{ads-H+} and k_{int} increase with decreasing pore size, causing k_{app} to also increase. Differences in K_{ads-H+} among the three zeolites are dominated by the values of ΔH_{ads-H+}, consistent with the original conclusion. This observation, however, is a consequence of the set of zeolites chosen for study; K_{ads-H+} for n-hexane adsorption in the zeolites employed for the present work is dominated by ΔS_{ads-H+}. Therefore, an increase in structural confinement does not, in general, lead to an increase in K_{ads-H+}. The results of this study also demonstrate that the methodology developed previously for extracting intrinsic rate parameters from measured data,[27] and improved herein, enables new insights to be made regarding the effects of confinement on alkane activation kinetics.

■ ASSOCIATED CONTENT

Ⓢ Supporting Information

The Supporting Information is available free of charge on the ACS Publications website at DOI: 10.1021/jacs.5b11355.

> Zeolite synthesis procedures, assessment of mass transfer limitations, details of CBMC simulations, analysis of uncertainties in activation parameters, and additional supporting data (PDF)
>
> Coordinates and crystal identification files (CIFs) for zeolite frameworks used for CBMC simulations (ZIP)

■ AUTHOR INFORMATION

Corresponding Author
*bell@cchem.berkeley.edu

Present Address
[⊥]L.-C.L.: Department of Materials Science and Engineering, Massachusetts Institute of Technology, 77 Massachusetts Avenue, Cambridge, MA 02139, USA.

Notes
The authors declare no competing financial interest.

■ ACKNOWLEDGMENTS

■ REFERENCES

(1) Corma, A. *Chem. Rev.* **1995**, *95*, 559–614.
(2) Primo, A.; Garcia, H. *Chem. Soc. Rev.* **2014**, *43*, 7548–7561.
(3) Kissin, Y. V. *Catal. Rev.: Sci. Eng.* **2001**, *43*, 85–146.
(4) Caeiro, G.; Carvalho, R. H.; Wang, X.; Lemos, M. A. N. D. A.; Lemos, F.; Guisnet, M.; Ramôa Ribeiro, F. *J. Mol. Catal. A: Chem.* **2006**, *255*, 131–158.
(5) Haag, W. O.; Dessau, R. M. Proceedings − International Congress on Catalysis, 8th, Berlin, Verlag Chemie: Weinheim, 1984; Vol. 2, pp 305−316.
(6) Kotrel, S.; Knözinger, H.; Gates, B. C. *Microporous Mesoporous Mater.* **2000**, *35−36*, 11−20.
(7) Bučko, T.; Benco, L.; Dubay, O.; Dellago, C.; Hafner, J. *J. Chem. Phys.* **2009**, *131*, 214508.
(8) Bučko, T.; Hafner, J. *J. Phys.: Condens. Matter* **2010**, *22*, 384201.
(9) Bučko, T.; Benco, L.; Hafner, J.; Ángyán, J. G. *J. Catal.* **2011**, *279*, 220−228.
(10) Zimmerman, P. M.; Tranca, D. C.; Gomes, J.; Lambrecht, D. S.; Head-Gordon, M.; Bell, A. T. *J. Am. Chem. Soc.* **2012**, *134*, 19468−19476.
(11) Konno, H.; Okamura, T.; Kawahara, T.; Nakasaka, Y.; Tago, T.; Masuda, T. *Chem. Eng. J. (Amsterdam, Neth.)* **2012**, *207−208*, 490−496.
(12) Voogd, P.; van Bekkum, H. *Appl. Catal.* **1990**, *59*, 311−331.
(13) Haag, W. O.; Lago, R. M.; Weisz, P. B. *Faraday Discuss. Chem. Soc.* **1981**, *72*, 317−330.
(14) Janda, A.; Bell, A. T. *J. Am. Chem. Soc.* **2013**, *135*, 19193−19207.
(15) Sharada, S. M.; Zimmerman, P. M.; Bell, A. T.; Head-Gordon, M. *J. Phys. Chem. C* **2013**, *117*, 12600−12611.
(16) Gounder, R.; Iglesia, E. *J. Am. Chem. Soc.* **2009**, *131*, 1958−1971.
(17) Bučko, T.; Hafner, J. *J. Catal.* **2015**, *329*, 32−48.
(18) van Bokhoven, J. A.; Xu, B. *Stud. Surf. Sci. Catal.* **2007**, *170*, 1167−1173.
(19) van Bokhoven, J. A.; Williams, B. A.; Ji, W.; Koningsberger, D. C.; Kung, H. H.; Miller, J. T. *J. Catal.* **2004**, *224*, 50−59.
(20) Babitz, S. M.; Williams, B. A.; Miller, J. T.; Snurr, R. Q.; Haag, W. O.; Kung, H. H. *Appl. Catal., A* **1999**, *179*, 71−86.
(21) Xu, B.; Sievers, C.; Hong, S. B.; Prins, R.; van Bokhoven, J. A. *J. Catal.* **2006**, *244*, 163−168.
(22) Ramachandran, C. E.; Williams, B. A.; van Bokhoven, J. A.; Miller, J. T. *J. Catal.* **2005**, *233*, 100−108.
(23) Gounder, R.; Iglesia, E. *Acc. Chem. Res.* **2012**, *45*, 229−238.
(24) Gounder, R.; Iglesia, E. *Chem. Commun. (Cambridge, U. K.)* **2013**, *49*, 3491−3509.
(25) Kotrel, S.; Rosynek, M. P.; Lunsford, J. H. *J. Phys. Chem. B* **1999**, *103*, 818−824.
(26) Derouane, E. G.; Chang, C. D. *Microporous Mesoporous Mater.* **2000**, *35−36*, 425−433.
(27) Janda, A.; Vlaisavljevich, B.; Lin, L.-C.; Sharada, M. S.; Smit, B.; Head-Gordon, M.; Bell, A. T. *J. Phys. Chem. C* **2015**, *119*, 10427−10438.
(28) Dědeček, J.; Sobalík, Z.; Wichterlová, B. *Catal. Rev.: Sci. Eng.* **2012**, *54*, 135−223.
(29) Liu, D.; Bhan, A.; Tsapatsis, M.; Al Hashimi, S. *ACS Catal.* **2011**, *1*, 7−17.
(30) Jones, A. J.; Carr, R. T.; Zones, S. I.; Iglesia, E. *J. Catal.* **2014**, *312*, 58−68.
(31) Narbeshuber, T. F.; Brait, A.; Seshan, K.; Lercher, J. A. *Appl. Catal., A* **1996**, *146*, 119−129.
(32) Al-majnouni, K. A.; Yun, J. H.; Lobo, R. F. *ChemCatChem* **2011**, *3*, 1333−1341.
(33) First, E. L.; Gounaris, C. E.; Wei, J.; Floudas, C. A. *Phys. Chem. Chem. Phys.* **2011**, *13*, 17339−17358.
(34) Dubbeldam, D.; Calero, S.; Vlugt, T. J. H.; Krishna, R.; Maesen, T. L. M.; Smit, B. *J. Phys. Chem. B* **2004**, *108*, 12301−12313.
(35) Dubbeldam, D.; Calero, S.; Vlugt, T. J. H.; Krishna, R.; Maesen, T. L. M.; Beerdsen, E.; Smit, B. *Phys. Rev. Lett.* **2004**, *93*, 088302.
(36) Martin, M. G.; Siepmann, J. I. *J. Phys. Chem. B* **1998**, *102*, 2569−2577.
(37) Swisher, J. A.; Hansen, N.; Maesen, T.; Keil, F. J.; Smit, B.; Bell, A. T. *J. Phys. Chem. C* **2010**, *114*, 10229−10239.
(38) Eder, F.; Stockenhuber, M.; Lercher, J. A. *J. Phys. Chem. B* **1997**, *101*, 5414−5419.
(39) Hunger, M. *Catal. Rev.: Sci. Eng.* **1997**, *39*, 345−393.

(40) Sarv, P.; Tuherm, T.; Lippmaa, E.; Keskinen, K.; Root, A. *J. Phys. Chem.* **1995**, *99*, 13763−13768.

(41) Willems, T. F.; Rycroft, C. H.; Kazi, M.; Meza, J. C.; Haranczyk, M. *Microporous Mesoporous Mater.* **2012**, *149*, 134−141.

(42) Barrer, R. M.; Davies, J. A. *Proc. R. Soc. London, Ser. A* **1971**, *322*, 1−19.

(43) Frenkel, D.; Smit, B. *Understanding Molecular Simulation: From Algorithms to Applications*, 2nd ed.; Computational Science Series, Vol. 1; Academic Press: New York, 2001; pp 173−176.

(44) Tranca, D. C.; Hansen, N.; Swisher, J.; Smit, B.; Keil, F. J. *J. Phys. Chem. C* **2012**, *116*, 23408−23417.

(45) De Moor, B. A.; Reyniers, M. F.; Gobin, O. C.; Lercher, J. A.; Marin, G. B. *J. Phys. Chem. C* **2011**, *115*, 1204−1219.

(46) Eder, F.; Lercher, J. A. *J. Phys. Chem. B* **1997**, *101*, 1273−1278.

(47) June, L. R.; Bell, A. T.; Theodorou, D. N. *J. Phys. Chem.* **1990**, *94*, 1508−1516.

(48) Yashonath, S.; Thomas, J. T.; Nowak, A. K.; Cheetham, A. K. *Nature* **1988**, *331*, 601−604.

(49) Jiang, T.; Göltl, F.; Bulo, R. E.; Sautet, P. *ACS Catal.* **2014**, *4*, 2351−2358.

(50) Zukal, A.; Mayerová, J.; Kubů, M. *Top. Catal.* **2010**, *53*, 1361−1366.

(51) Li, X.; Liu, X.; Liu, S.; Xie, S.; Zhu, X.; Chen, F.; Xu, L. *RSC Adv.* **2013**, *3*, 16549−16557.

(52) Wang, L.; Tian, P.; Yuan, Y.; Yang, M.; Fan, D.; Zhou, H.; Zhu, W.; Xu, S.; Liu, Z. *Microporous Mesoporous Mater.* **2014**, *196*, 89−96.

(53) Song, W.; Liu, Z.; Liu, L.; Skov, A. L.; Song, N.; Xiong, G.; Zhu, K.; Zhou, X. *RSC Adv.* **2015**, *5*, 31195−31204.

(54) Goel, S.; Zones, S. I.; Iglesia, E. *Chem. Mater.* **2015**, *27*, 2056−2066.

(55) Carpenter, J. R.; Yeh, S.; Zones, S. I.; Davis, M. E. *J. Catal.* **2010**, *269*, 64−70.

(56) Zones, S. I.; Hwang, S.-J.; Davis, M. E. *Chem. - Eur. J.* **2001**, *7*, 1990−2001.

(57) Verboekend, D.; Chabaneix, A. M.; Thomas, K.; Gilson, J.-P.; Pérez-Ramírez, J. *CrystEngComm* **2011**, *13*, 3408−3416.

(58) Hayasaka, K.; Liang, D.; Huybrechts, W.; De Waele, B. R.; Houthoofd, K. J.; Eloy, P.; Gaigneaux, E. M.; van Tendeloo, G.; Thybaut, J. W.; Marin, G. B.; Denayer, J. F. M.; Baron, G. V.; Jacobs, P. A.; Kirschhock, C. E. A.; Martens, J. A. *Chem. - Eur. J.* **2007**, *13*, 10070−10077.

(59) Denayer, J. F. M.; Ocakoglu, R. A.; Thybaut, J.; Marin, G.; Jacobs, P.; Martens, J.; Baron, G. V. *J. Phys. Chem. B* **2006**, *110*, 8551−8558.

(60) June, R. L.; Bell, A. T.; Theodorou, D. N. *J. Phys. Chem.* **1992**, *96*, 1051−1060.

(61) Smit, B.; Siepmann, J. I. *J. Phys. Chem.* **1994**, *98*, 8442−8452.

(62) Bates, S. P.; van Well, W. J. M.; van Santen, R. A.; Smit, B. *J. Phys. Chem.* **1996**, *100*, 17573−17581.

(63) Bates, S. P.; van Well, W. J. M.; van Santen, R. A.; Smit, B. *Mol. Simul.* **1997**, *19*, 301−318.

(64) Savitz, S.; Siperstein, F.; Gorte, R. J.; Myers, A. L. *J. Phys. Chem. B* **1998**, *102*, 6865−6872.

(65) Derycke, I.; Vigneron, J. P.; Lambin, P.; Lucas, A. A.; Derouane, E. G. *J. Chem. Phys.* **1991**, *94*, 4620−4627.

(66) Baerlocher, C.; Weber, T.; McCusker, L. B.; Palatinus, L.; Zones, S. I. *Science* **2011**, *333*, 1134−1137.

(67) Eder, F.; Lercher, J. A. *Zeolites* **1997**, *18*, 75−81.

(68) Solans-Monfort, X.; Sodupe, M.; Mó, O.; Yáñez, M.; Elguero, J. *J. Phys. Chem. B* **2005**, *109*, 19301−19308.

(69) Solans-Monfort, X.; Sodupe, M.; Branchadell, V.; Sauer, J.; Orlando, R.; Ugliengo, P. *J. Phys. Chem. B* **2005**, *109*, 3539−3545.

(70) Katada, N.; Sota, S.; Morishita, N.; Okumura, K.; Niwa, M. *Catal. Sci. Technol.* **2015**, *5*, 1864−1869.

(71) Barrie, P. J. *Phys. Chem. Chem. Phys.* **2012**, *14*, 318−326.

(72) Norwisz, J.; Smieszek, Z.; Kolenda, Z. *Thermochim. Acta* **1989**, *156*, 313−320.

(73) Gallicchio, E.; Kubo, M.; Levy, R. M. *J. Am. Chem. Soc.* **1998**, *120*, 4526−4527.

(74) Liu, L.; Guo, Q.-X. *Chem. Rev.* **2001**, *101*, 673−695.

(75) Snyder, P. W.; Lockett, M. R.; Moustakas, D. T.; Whitesides, G. M. *Eur. Phys. J.: Spec. Top.* **2014**, *223*, 853−891.

(76) Bond, G. C.; Keane, M. A.; Kral, H.; Lercher, J. A. *Catal. Rev.: Sci. Eng.* **2000**, *42*, 323−383.

(77) Ryde, U. *MedChemComm* **2014**, *5*, 1324−1336.

(78) Dunitz, J. D. *Chem. Biol. (Oxford, U. K.)* **1995**, *2*, 709−712.

(79) Lercher, J. A. *Stud. Surf. Sci. Catal.* **1999**, *123*, 543−566.

(80) Conner, W. C., Jr. *J. Catal.* **1982**, *78*, 238−246.

(81) *Ohio Supercomputer Center*, http://osc.edu/ark:/19495/f5s1ph73, 1987.